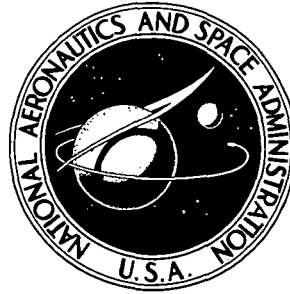


**NASA CONTRACTOR
REPORT**



NASA CR-2366

NASA CR-2366

**EVALUATION OF A SERIES HYBRID
THRUST BEARING AT DN VALUES
TO THREE MILLION**

I - Analysis and Design

by A. Gu, M. Eusepi, and L. W. Winn

Prepared by

MECHANICAL TECHNOLOGY INCORPORATED

Latham, N.Y. 12110

for Lewis Research Center

NATIONAL AERONAUTICS AND SPACE ADMINISTRATION • WASHINGTON, D. C. • JANUARY 1974

1. Report No. NASA CR-2366		2. Government Accession No.		3. Recipient's Catalog No.	
4. Title and Subtitle EVALUATION OF A SERIES HYBRID THRUST BEARING AT DN VALUES TO THREE MILLION I - ANALYSIS AND DESIGN				5. Report Date January 1974	
				6. Performing Organization Code	
7. Author(s) A. Gu, M. Eusepi, and L. W. Winn				8. Performing Organization Report No. MTI-73TR10	
9. Performing Organization Name and Address Mechanical Technology Incorporated 968 Albany-Shaker Road Latham, New York 12110				10. Work Unit No.	
				11. Contract or Grant No. NAS 3-16740	
				13. Type of Report and Period Covered Contractor Report	
12. Sponsoring Agency Name and Address National Aeronautics and Space Administration Washington, D. C. 20546				14. Sponsoring Agency Code	
15. Supplementary Notes Final Report. Project Manager, Herbert W. Scibbe, Fluid System Components Division, NASA Lewis Research Center, Cleveland, Ohio					
16. Abstract This report presents the analysis and design of a hybrid bearing consisting of a 150-mm ball bearing and a centrifugally actuated, conical, fluid film bearing fitting an envelope with an outer radius of 86.4 mm (3.4 in.) and an inner radius of 71 mm (2.8 in.). The bearing analysis, combined with available torque data on ball bearings, indicates that an effective speed split between the ball and fluid-film bearings of 50 percent may be expected during operation at 20,000 rpm and under an axial load of 17,800 newtons (4000 lbs.). This speed split can result in a ten-fold increase in the life of the ball bearing when compared to a simple ball bearing system operating under similar conditions.					
17. Key Words (Suggested by Author(s)) Bearings; Ball bearing; Conical hydrostatic bearing; Series hybrid thrust bearing				18. Distribution Statement Unclassified - unlimited	
19. Security Classif. (of this report) Unclassified		20. Security Classif. (of this page) Unclassified		21. No. of Pages 53	
				22. Price* Domestic, \$3.50 Foreign, \$6.00	

TABLE OF CONTENTS

	<u>Page</u>
SUMMARY _____	1
INTRODUCTION _____	2
HYBRID BEARING DESIGN _____	3
Hydrostatic Fluid-Film Bearing Design _____	3
Ball Bearing Configuration _____	25
Series Hybrid Thrust Bearing Performance _____	25
Thermal Analysis _____	31
Thermoelastic Deformation Analysis _____	31
CRITICAL SPEED ANALYSIS _____	40
DESCRIPTION OF BEARING AND TEST VEHICLE _____	42
CONCLUSIONS _____	45
NOMENCLATURE _____	46
REFERENCES _____	48

LIST OF FIGURES

	<u>Page</u>
1 SCHEMATIC DIAGRAMS OF CONICAL HYDROSTATIC BEARING DESIGN-----	4
2 EFFECT OF FLOW RATE ON RADIUS RATIO X_2 FOR OPTIMAL BEARING. DIMENSIONLESS LAMINAR FRICTION COEFFICIENT, O .-----	7
3 TORQUE VERSUS SPEED RATIO-----	11
4 TORQUE VERSUS SPEED RATIO-----	12
5 TORQUE VERSUS SPEED RATIO-----	13
6 LOAD VERSUS FILM THICKNESS-----	14
7 LOAD VERSUS FILM THICKNESS-----	15
8 LOAD VERSUS FILM THICKNESS-----	16
9 OFF DESIGN SPEED PERFORMANCE, LOAD AND FLOW VERSUS FILM THICKNESS-----	17
10 OFF DESIGN SPEED PERFORMANCE, LOAD AND FLOW VERSUS FILM THICKNESS-----	18
11 OFF DESIGN SPEED PERFORMANCE, LOAD AND FLOW VERSUS FILM THICKNESS-----	19
12 SPEED SPLIT OF SERIES HYBRID THRUST BEARING, SPEED = 20,000 RPM-----	21
13 SPEED SPLIT OF SERIES HYBRID THRUST BEARING, SPEED = 15,000 RPM-----	22
14 SPEED SPLIT OF SERIES HYBRID THRUST BEARING, SPEED = 10,000 RPM-----	23
15 AXIAL STIFFNESS OF FLUID-FILM BEARING-----	24
16 MATHEMATICAL MODEL FOR HEAT TRANSFER-----	32
17 TEMPERATURE DISTRIBUTION IN SERIES HYBRID BEARING-----	34

LIST OF FIGURES (cont'd.)

	<u>Page</u>
18 THERMOELASTIC MODEL FOR FLUID-FILM BEARING	
PRIMARY ROTOR-----	35
19 ANALYTICAL MODEL FOR THE INTERMEDIATE ROTOR-----	38
20 FLUID-FILM BEARING STIFFNESS-----	41
21 TEST HEAD LAYOUT-----	43

LIST OF TABLES

	<u>Page</u>
I. BALL BEARING TORQUE CHARACTERISTICS-----	26
II. BALL BEARING RADIAL STIFFNESS-----	27
III. DIFFERENTIAL SPEED DATA-----	29
IV. TORQUE AND LIFE COMPARISON BETWEEN SINGLE AND HYBRID BEARINGS-----	30
V. THERMAL MODEL SPECIFICATIONS FOR SERIES HYBRID BOOST BEARING-----	33
VI. INPUT PARAMETERS, PRIMARY ROTOR DISTORTION ANALYSIS-----	37
VII. INPUT PARAMETERS, INTERMEDIATE ROTOR DISTORTION ANALYSIS-----	37
VIII. SUMMARY OF DISTORTIONS, FLUID-FILM BEARING-----	39

SUMMARY

The design of a Series Hybrid Bearing, consisting of a combination of a ball and fluid-film bearing, was carried out to determine the improvement in ball bearing fatigue life that can be achieved through a reduction in the rotational speed of the ball bearing. Within the scope of this program, a 150-mm ball bearing was coupled in series with a centrifugally actuated, conical, fluid-film bearing fitting an envelope of an outer radius of 86.4 mm (3.4 in.) and an inner radius of 71 mm (2.8 in.). The design and optimization studies of the fluid-film bearing yielded a bearing which theoretically meets all of the stipulated requirements. The torque data for the ball bearing, when combined with that for the fluid-film bearing, indicated a very favorable speed split between the two. The speed ratio at the design point of 17,800 newtons (4000 lbs.) axial load and 20,000 rpm is approximately 0.50, indicating that the ball bearing will be operating at one-half the rotor speed at these conditions. This speed split can result in a ten-fold increase in the life of the ball bearing when compared to a simple ball bearing system operation under similar conditions.

I. INTRODUCTION

The use of low-mass, hollow or drilled balls in high-speed bearings, to reduce contact stress and thereby improve fatigue life, has been demonstrated with limited success at the Lewis Research Center. Another method for improving fatigue life of the ball bearing is to reduce its rotational speed by coupling it in series with a fluid-film bearing. This arrangement is called a Series Hybrid Bearing. The Series Hybrid Bearing has several advantages when compared to the hollow and drilled ball bearing concepts at DN values between 3 and 4 million. Two of these advantages, a greater bearing life improvement potential and the built-in "fail-safe" feature of the backup ball bearing, make the Series Hybrid Bearing a very attractive high-speed bearing concept.

The work discussed in this report was performed under a contract with NASA Lewis Research Center, Contract No. NAS3-16740, and represents the results of the design effort. The second portion of the program will include the fabrication of a test vehicle and the performance of tests on the Series Hybrid Bearing to obtain practical verification of the analytical predictions. The work to be performed in the second portion will be reported upon at a later date.

II. HYBRID BEARING DESIGN

A. Hydrostatic Fluid-Film Bearing Design

The objective is to determine the geometrical dimensions and oil feeding arrangements of the conical hydrostatic fluid-film bearing that yields minimum friction torque. The schematic of the hydrostatic bearing system is shown in Figure 1. According to the statement of work, the hydrostatic bearing must satisfy the following conditions:

- The outer radius $R_4 \leq 84.8$ mm (3.34 in.) and the inner radius $R_1 \geq 71.4$ mm (2.81 in.)
- The bearing angle $\theta = 45^\circ$.
- The design oil viscosity $\mu = 5.5 \times 10^{-3}$ newtons per sec: per square meter (8×10^{-7} lb-sec/in²) and the oil density $\rho = 9.4 \times 10^2$ Kilograms per cubic meter (0.034 lb/in³).
- At design speed $\omega_s = 20,000$ rpm and design load $F = 17,800$ newtons (4000 lbs.) the fluid-film bearing friction torque is a minimum.
- At design speed $\omega_s = 20,000$ rpm and at a load of 4450 newtons (1000 lbs.) the oil flow rate $Q \leq 37.9$ liters per min. (10 gpm).

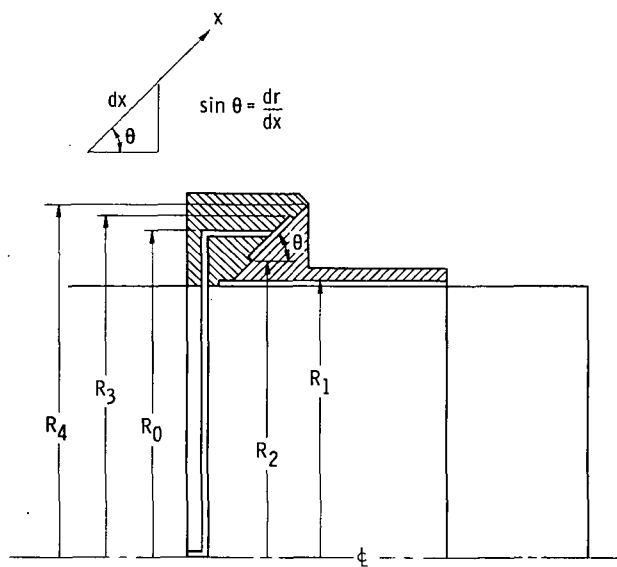
Optimized bearing data for conical hydrostatic bearings for minimum friction were compiled by Nypan, et al (Reference 1) based on their computer solutions. The following design analysis makes extensive use of the data presented in Reference 1. Orifice feeding to the bearing pockets is assumed.

1. Analytical Background

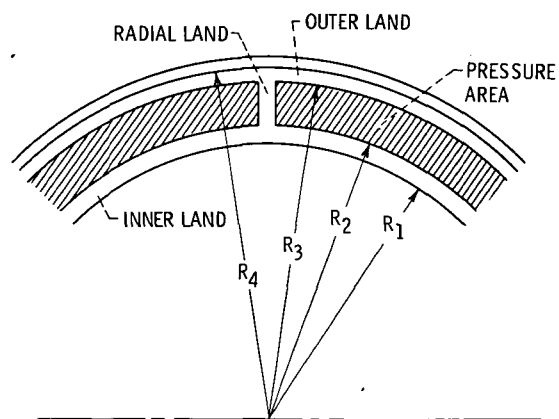
Following the analysis given in the cited reference, the dimensionless thrust load and flow rate are:

$$\bar{F} = X_4^2 + X_3^2 - X_2^2 - 1 \quad (1)$$

$$\bar{Q} = \frac{1}{\ln X_2} + \frac{1}{\ln \frac{X_4}{X_3}} \quad (2)$$



(a) SECTION VIEW.



(b) FRONT VIEW.

Fig. 1 Schematic diagrams of conical hydrostatic bearing design.

where

$$\bar{F} = \frac{F}{\pi p R_1^2} \quad (3)$$

$$\bar{Q} = \frac{6\mu Q}{\pi p h_L^3 \sin\theta} \quad (4)$$

$$X_i = \frac{R_i}{R_1} \quad (5)$$

and F is the thrust load, Q the flow rate, p the pocket pressure, h_L the land clearance, μ the fluid viscosity, and θ the cone angle (45° for the present case).

The friction torque M_L consists of the torque M_L due to the laminar shearing of the fluid between inner and outer circumferential lands and the mating surface and the friction torque M_p , resulting from the shearing of the fluid in the bearing pockets which may be laminar or turbulent depending on the relative rotational speed. M_L can be expressed as,

$$\bar{M}_L = X_4^4 - X_3^4 + X_2^4 - 1 \quad (6)$$

where

$$\bar{M}_L = \frac{2h_L \sin\theta M_L}{\pi \mu (\omega_s - \omega_b) R_1^4} \quad (7)$$

and ω_s is the shaft speed and ω_b the ball bearing speed. The pocket friction M_p depends on the Reynolds number defined by

$$R_e = \frac{\rho R_2 (\omega_s - \omega_b) h_p}{\mu} \quad (8)$$

where h_p is the pocket depth. The expression for the normalized pocket friction torque for laminar flow is

$$\bar{M}_p = C_1 (X_3^4 - X_2^4) \text{ for } R_e \leq 1000 \quad (9)$$

where

$$C_1 = 4 f_r \frac{h_L}{h_p} \quad (10)$$

and f_r is the fraction of area between R_2 and R_3 occupied by hydrostatic pockets (f_r is close to one for the present case). For turbulent flow, the normalized torque is

$$\bar{M}_p = C_2 (X_4^{4.75} - X_2^{4.75}) \text{ for } R_e > 1000 \quad (11)$$

where

$$C_2 = \frac{0.124}{4.75} f_r \left[\rho \frac{R_1 (\omega_s - \omega_b) h_p}{\mu} \right]^{0.75} \frac{h_L}{h_p} \quad (12)$$

For given load \bar{F} and flow \bar{Q} , values of X_2 , X_3 , and X_4 that yield a minimum total friction torque \bar{M}_t are given in the reference in graphical form. Actually, X_2 , X_3 , and X_4 are related through Equations (1) and (2). Therefore, X_2 may be considered as the only dependent variable and, X_3 and X_4 may be expressed in terms of \bar{F} , \bar{Q} , and X_2 as:

$$X_3^2 = \frac{\bar{F} + X_2^2 + 1}{2} \frac{1}{1 + \exp\left(\bar{Q} - \frac{1}{\ln X_2}\right)} \quad (13)$$

and

$$X_4 = X_3 \exp\left(\bar{Q} - \frac{1}{\ln X_2}\right) \quad (14)$$

The relationship between the optimal value of X_2 and \bar{F} and \bar{Q} is shown in Figure 2, which was reproduced from Reference 1.

For a given design load, the value of \bar{F} depends on the level of pocket pressure p (see Equation (3)). Pocket pressure p , as will be shown later, is a function of the orifice restriction, bearing geometry, and clearance. Thus, for a given design load, the factors affecting pocket pressure have to be established.

For this hydrostatic, fluid-film bearing in the series hybrid bearing system, oil is fed to the bearing pockets centrifugally. The supply pressure is, therefore

$$p_s = \frac{1}{2} \rho R_o^2 \omega_s^2 \quad (15)$$

where R_o is the radius defining the location of the feeding orifices. Using Bernoulli's equation, the flow rate through the orifices is

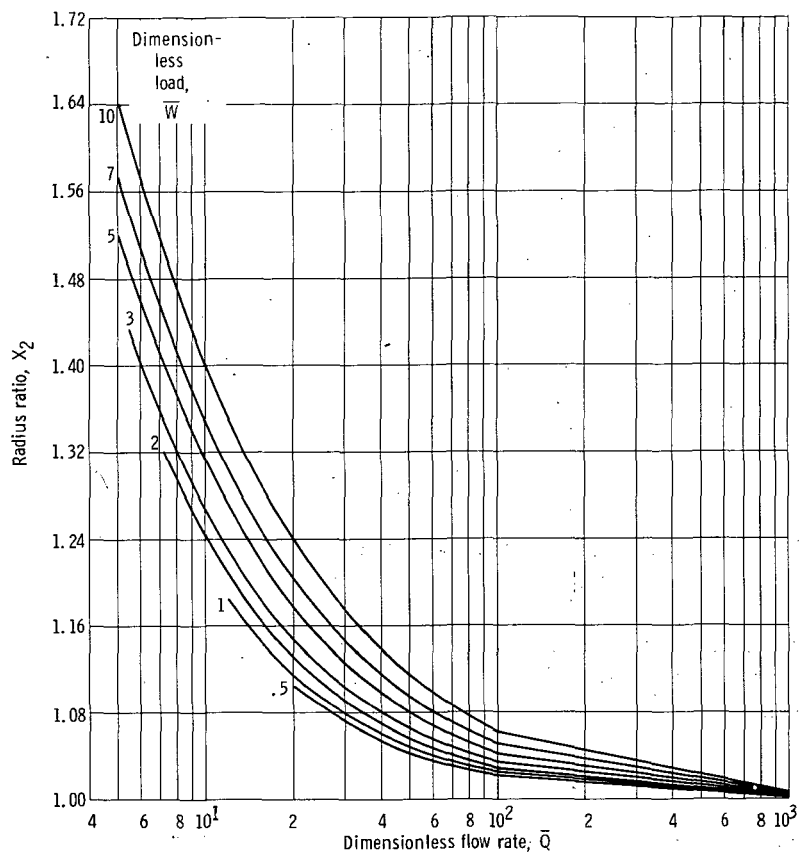


Fig. 2 Effect of flow rate on radius ratio X_2 for optimal bearing. Dimensionless laminar friction coefficient, 0.

$$Q = C_d n \pi d^2 \frac{1}{2} \left[\frac{2 (p_s - p)}{\rho} \right]^{1/2} \quad (16)$$

where n is the number of orifices, d the orifice diameter, p the pocket pressure downstream of the orifices, and C_d the orifice discharge coefficient accounting for any deviation from ideal orifice flow. Continuity requires that the orifice flow rate must be equal to the flow rate through the bearing clearance. This requirement gives rise to the expression for the pocket pressure as follows:

$$\frac{\bar{p}}{p_s} = \frac{-1 + (1 + 4k^2)^{1/2}}{2k^2} \quad (17)$$

where

$$\frac{\bar{p}}{p_s} = \frac{p}{p_s} \quad (18)$$

$$k = \left[\frac{2\rho p_s}{9} \right]^{1/2} \frac{h_L^3 \sin\theta}{C_d n d^2 \mu} \left[\frac{1}{\ln X_2} + \frac{1}{\ln \frac{X_4}{X_3}} \right] \quad (19)$$

k may be considered as the ratio of the orifice flow resistance to the fluid-film flow resistance.

The procedure of using the available data given in the reference to select a bearing configuration for minimum friction is described below.

2. Bearing Configuration Selection Procedure

In order to use the bearing data given in the reference effectively, the following scheme has been employed and automated on a digital computer. The selection of the optimized bearing configuration was performed on the basis of minimum friction.

Procedure

1. Set $R_1 = 71.4$ mm (2.81 in.) (the minimum value) for minimum friction.
2. Assume a reasonable R_o ($R_3 > R_o > R_2$) so that p_s can be calculated from Equation (15) by letting ω_s be the design speed of 20,000 rpm.

3. Assume a value of \bar{p} ($0 < \bar{p} < 1$) so that p and \bar{F} corresponding to the design load of 17,800 newtons (4000 lbs.) can be calculated.
4. Assume a value of X_2 ($1 < X_2 < X_4$ and $X_4 < \frac{3.34}{2.81} = 1.19$). Using the relation among X_2, \bar{F} and \bar{Q} given in Figure 2 (\bar{Q}) corresponding to $F = 17,800$ newtons (4000 lbs.) is obtained. \bar{Q} as a function of \bar{F} and X_2 is stored in the selection computer program as a two-dimensional numerical table.
5. From (\bar{F}) , (\bar{Q}) and X_2 , X_3 and X_4 are obtained from Equations (13) and (14).
6. Compute the flow resistance ratio (k) corresponding to $F = 17,800$ newtons (4000 lbs.) by using Equation (17). Then calculate $(h_L)/C_d n d^2$ from Equation (19).
7. From \bar{F} and $F = 4450$ newtons (1000 lbs.), compute the corresponding p and \bar{p} .
8. Calculate (k) and $(h_L)^3/C_d n d^2$ similar to step 6.
9. Using Equation (16) and setting $(Q) = 37.9$ liters/min. (10 gpm), calculate the maximum value for $C_d n d^2$ to satisfy the flow requirement.
10. Let $C_d n d^2$ be equal to the obtained maximum value for minimum friction. Compute (h_L) . Thus, the bearing configuration is completely defined for $F = 17,800$ newtons (4000 lbs.) and 4450 newtons (1000 lbs.).
11. Compute the bearing friction torque for different values of ball bearing speed ω_b ranging from 0 to ω_s .

The bearing dimensions selected represent an optimized configuration for the assumed \bar{F} and \bar{Q} . For a complete selection, all possible values of \bar{F} and \bar{Q} should be covered. To accomplish this in the selection computer program, steps 4 to 11 form an inner loop for variation in \bar{Q} for a given \bar{F} ; while steps 3 to 11 form an outer loop covering all possible \bar{F} .

Since the bearing friction torque is approximately proportional to the bearing radius raised to the fourth power or higher (see Equation (6) and (11)), small bearings yield low torques. For a given load, a small bearing requires high pocket pressure and from Equation (3), the corresponding dimensionless load \bar{F} is small. The available optimized bearing data, shown in Figure 2, only covers \bar{F} from 0.5 to 10. $\bar{F} = 0.5$ corresponds to $\bar{p} = 0.377$ (pocket pressure is 37.7 percent of supply pressure). In the bearing configuration selection process, for $\bar{p} > 0.377$

($\bar{F} < 0.5$) the optimized bearing configurations were obtained by linear extrapolation of the available data given in Figure 2. Exact bearing data for low values of \bar{F} in the range of 0.1 and 0.5 were later supplied by the NASA Project Manager. The exact data have been shown to be in good agreement with the linear extrapolation.

The above procedure yields a series of "optimized" bearing configurations. A final absolute optimized bearing was then chosen from those configurations by considering:

- Bearing stiffness at the design load and design speed
- Bearing stiffness characteristics at off-design conditions
- Oil flow rates
- Bearing friction torques at different loads and speeds
- Manufacturability in terms of the values of R_1, R_2, R_3, R_4, h_L and nd^2

3. The Selected Bearing

Figures 3 through 5 show three optimized bearing configurations for $\bar{p} = 0.3, 0.4$, and 0.5 respectively. The bearing dimensions are identified in the figures. The figures plot the bearing torques as functions of the ball bearing speed to shaft ratio ω_b/ω_s , with the pocket depth ratio h_p/h_L as the third parameter. Also cross-plotted for reference is MTI ball bearing torque data obtained at a thrust load of 8900 newtons (2000 lbs.). The intersection shows the equilibrium ball bearing speed for the given load. Although the torque level is, in general, higher for smaller \bar{p} due to the large bearing size required. The equilibrium points, e.g., for $h_p/h_L = 100$, are all in the range of $0.6 < \omega_b/\omega_s < 0.65$. The difference in ball bearing speed reduction among the three bearings thus seems small.

The bearing clearances at the design load are largest for the case of $\bar{p} = 0.3$. The load and flow versus clearance curves at the design speed of 20,000 rpm for the three bearings are shown in Figures 6 through 8. It appears that all three bearings have good stiffness in the design-load range and the flow rates are also comparable. Figures 9 through 11 plot the load flow curves at lower speeds of 15,000 and 10,000 rpm for the three bearings, respectively. At these conditions, the bearing corresponding to $\bar{p} = 0.3$ has the best stiffness characteristics. Because of the high load carrying capacity at off-design conditions and good performance in terms of stiffness, flow and film thickness at the design point, a $\bar{p} = 0.3$ was selected.

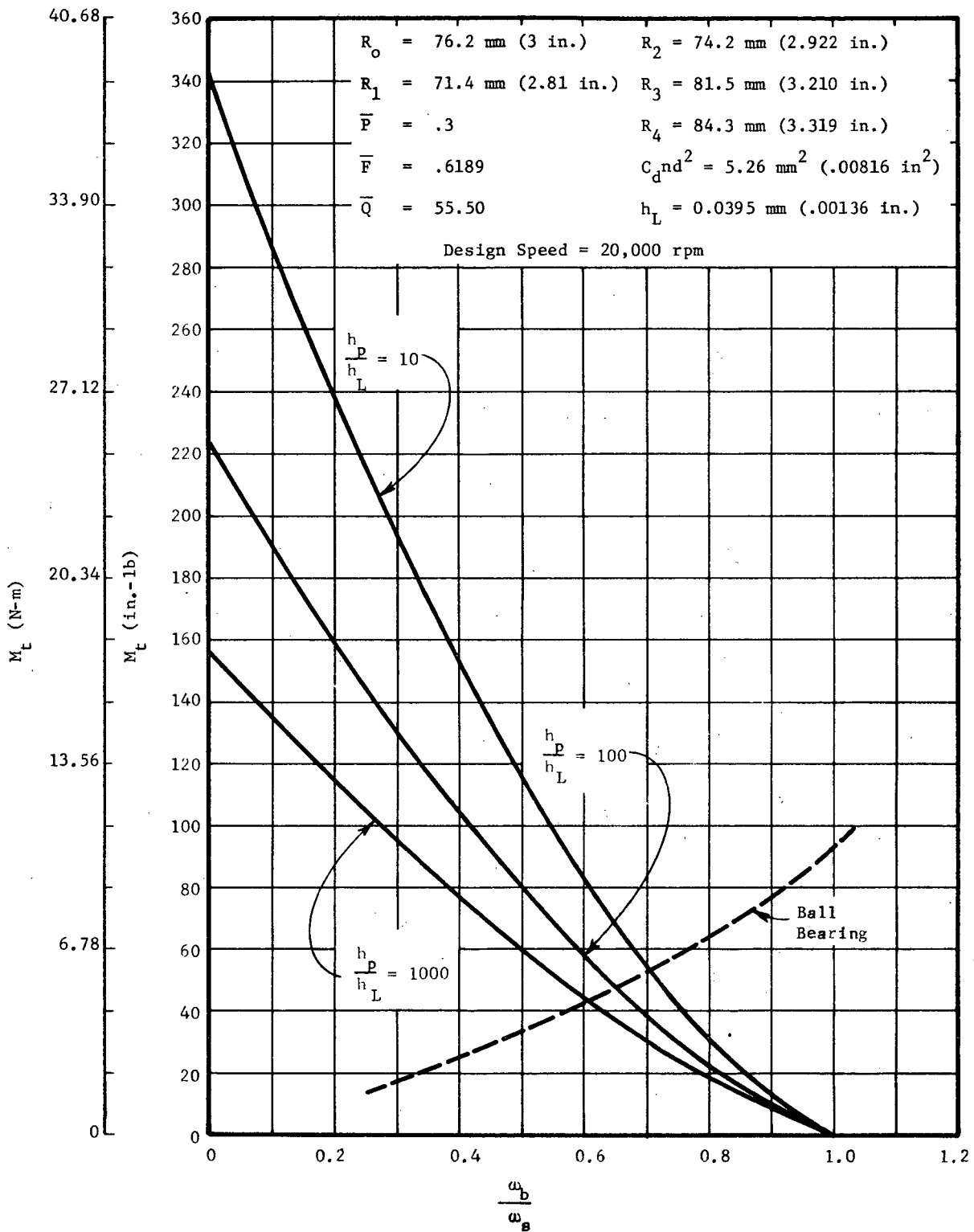


Fig. 3 Torque vs. Speed Ratio

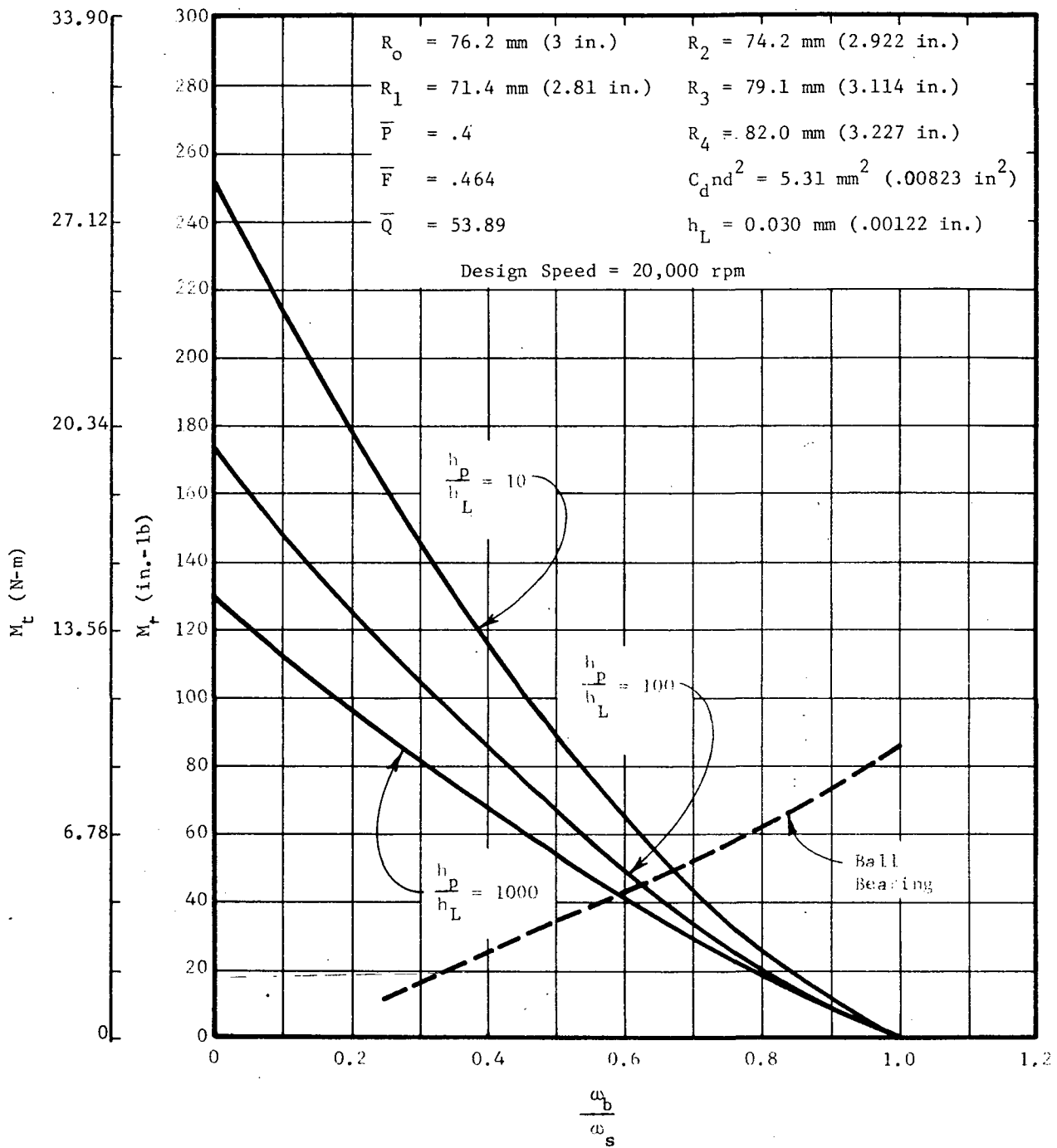


Fig. 4 Torque vs. Speed Ratio

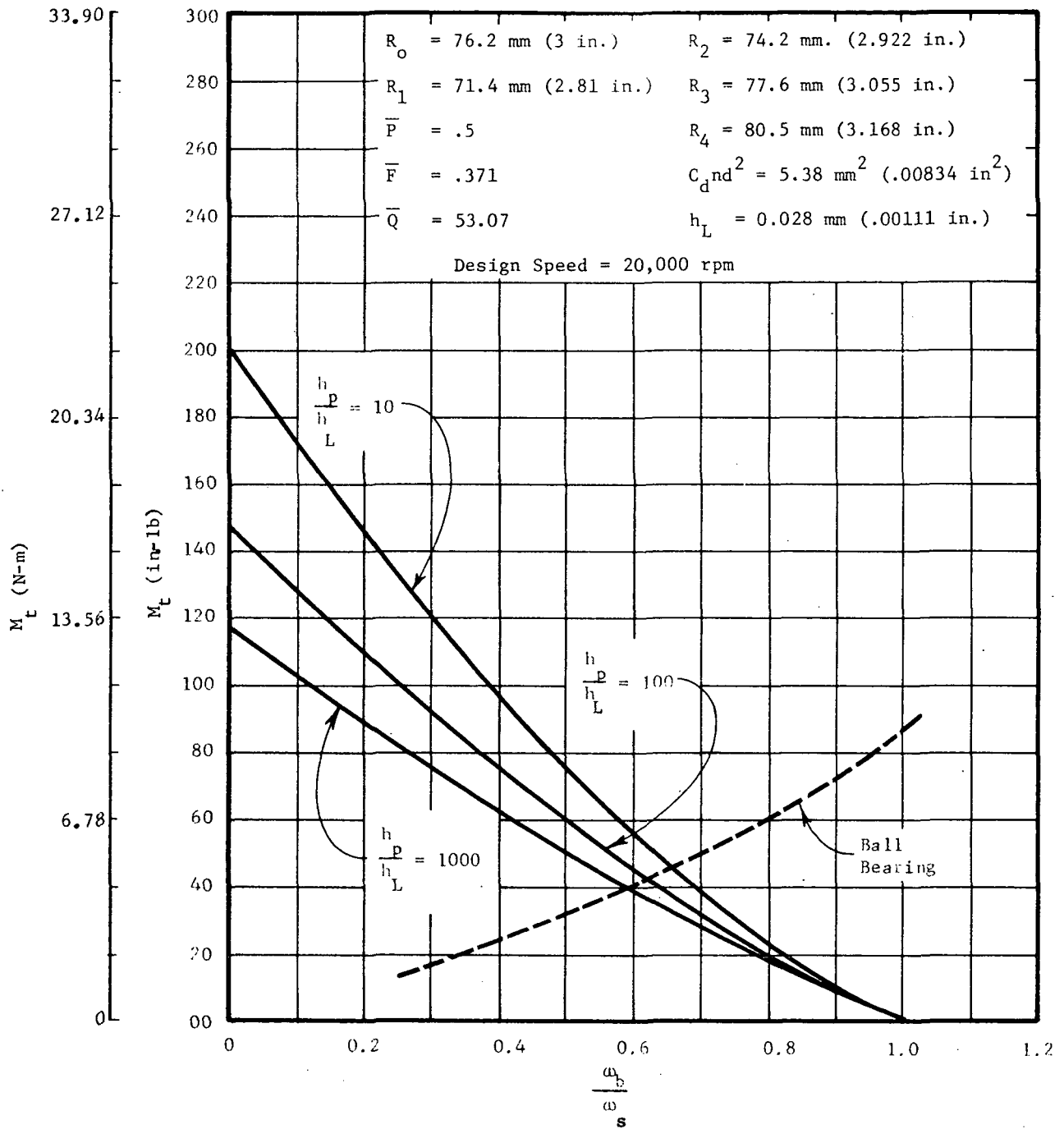


Fig. 5 Torque vs. Speed Ratio

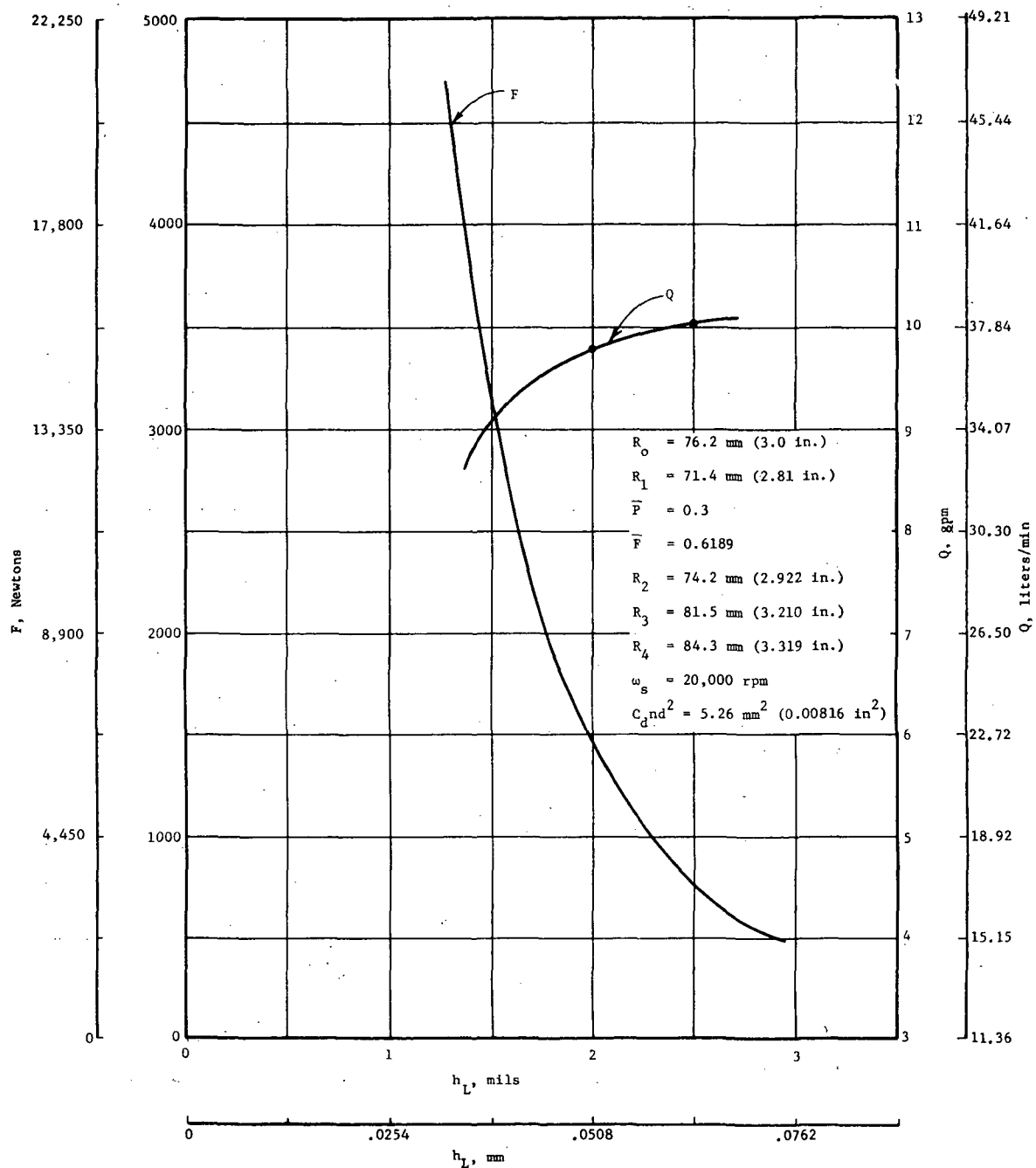


Fig. 6 Load Versus Film Thickness

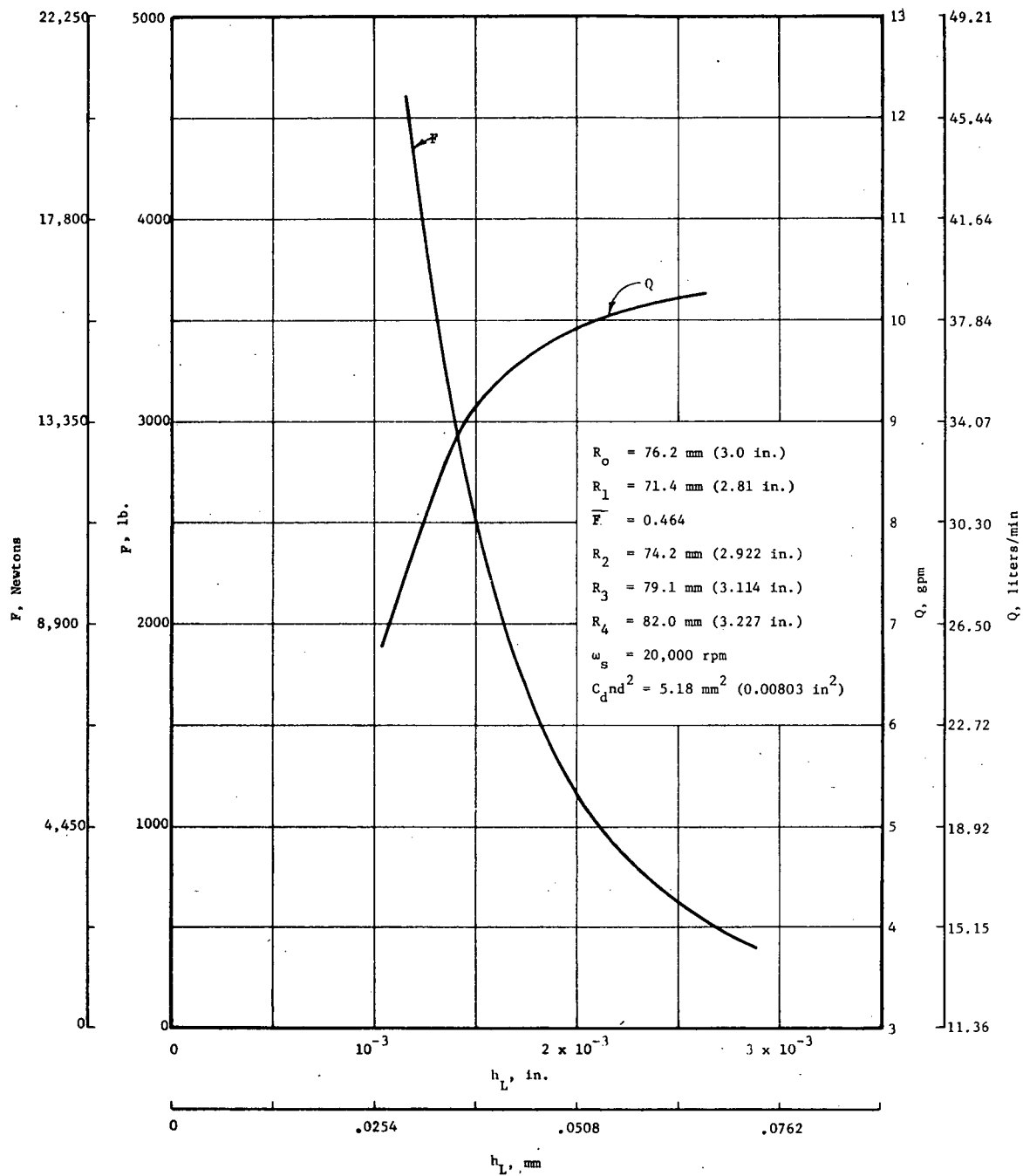


Fig. 7 Load Versus Film Thickness

$$\bar{p} = 0.4$$

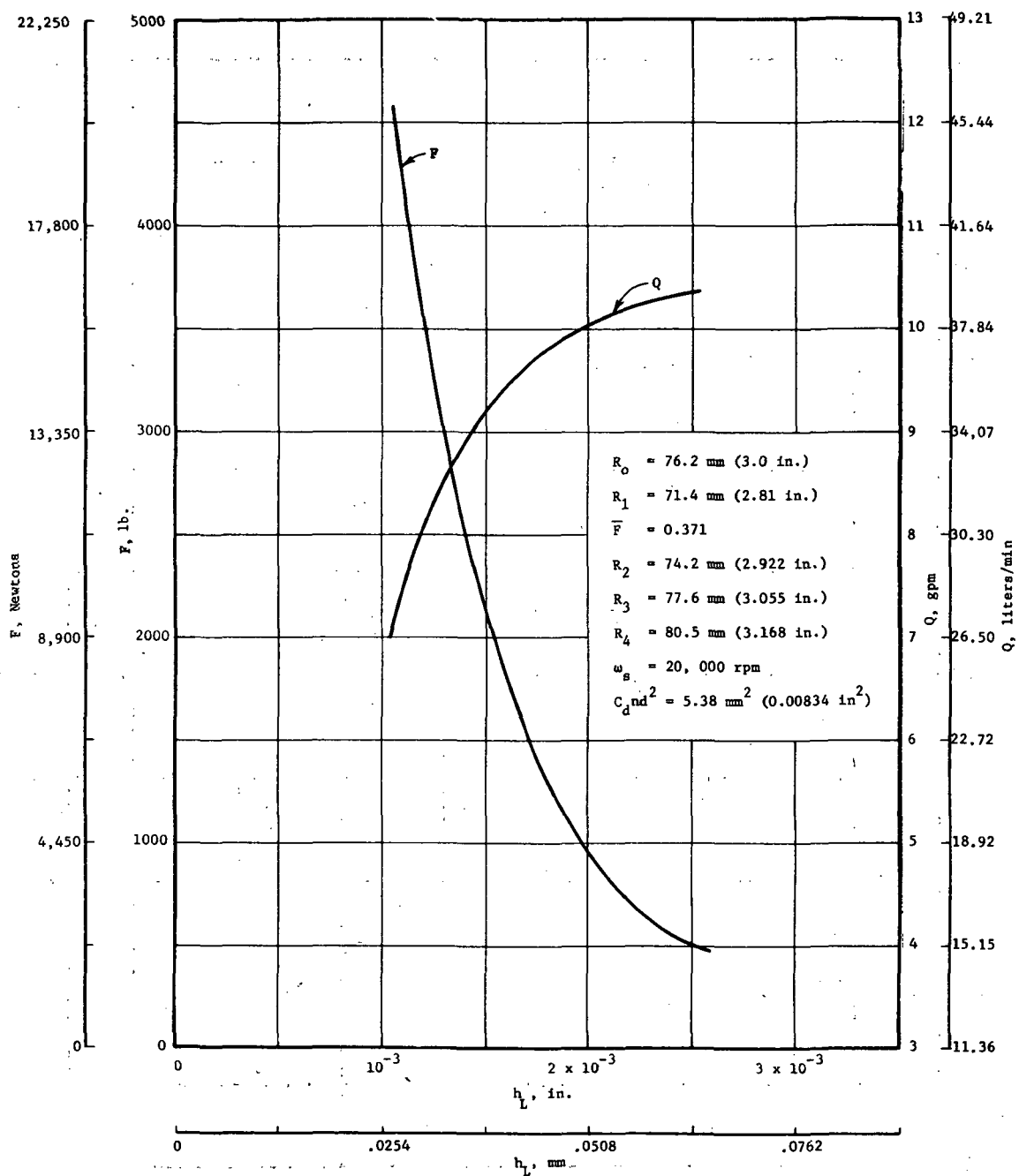


Fig. 8 Load Versus Film Thickness

$$\bar{p} = 0.5$$

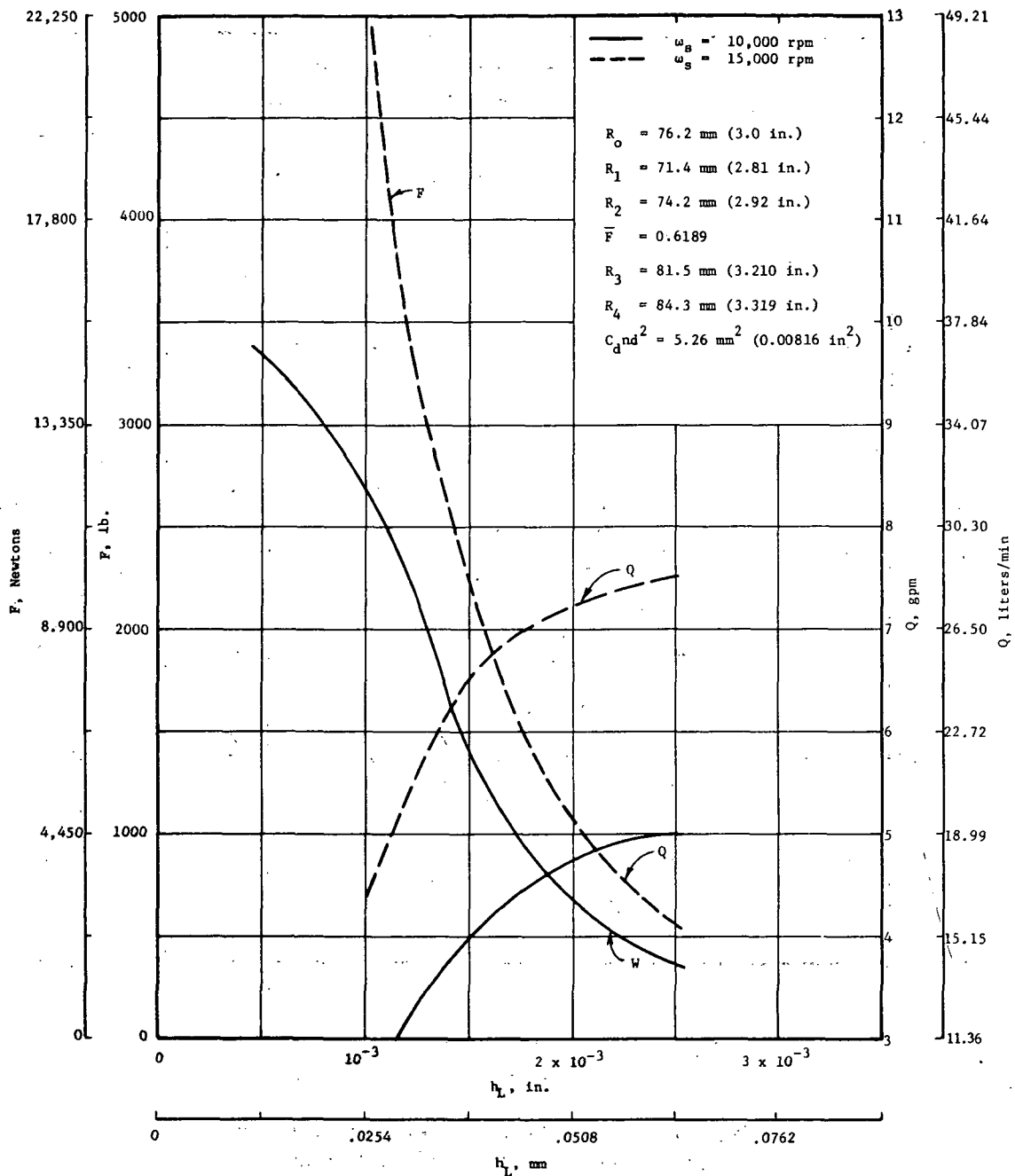


Fig. 9 Off Design Speed Performance
Load and Flow vs. Film Thickness

$$\bar{p} = 0.3$$

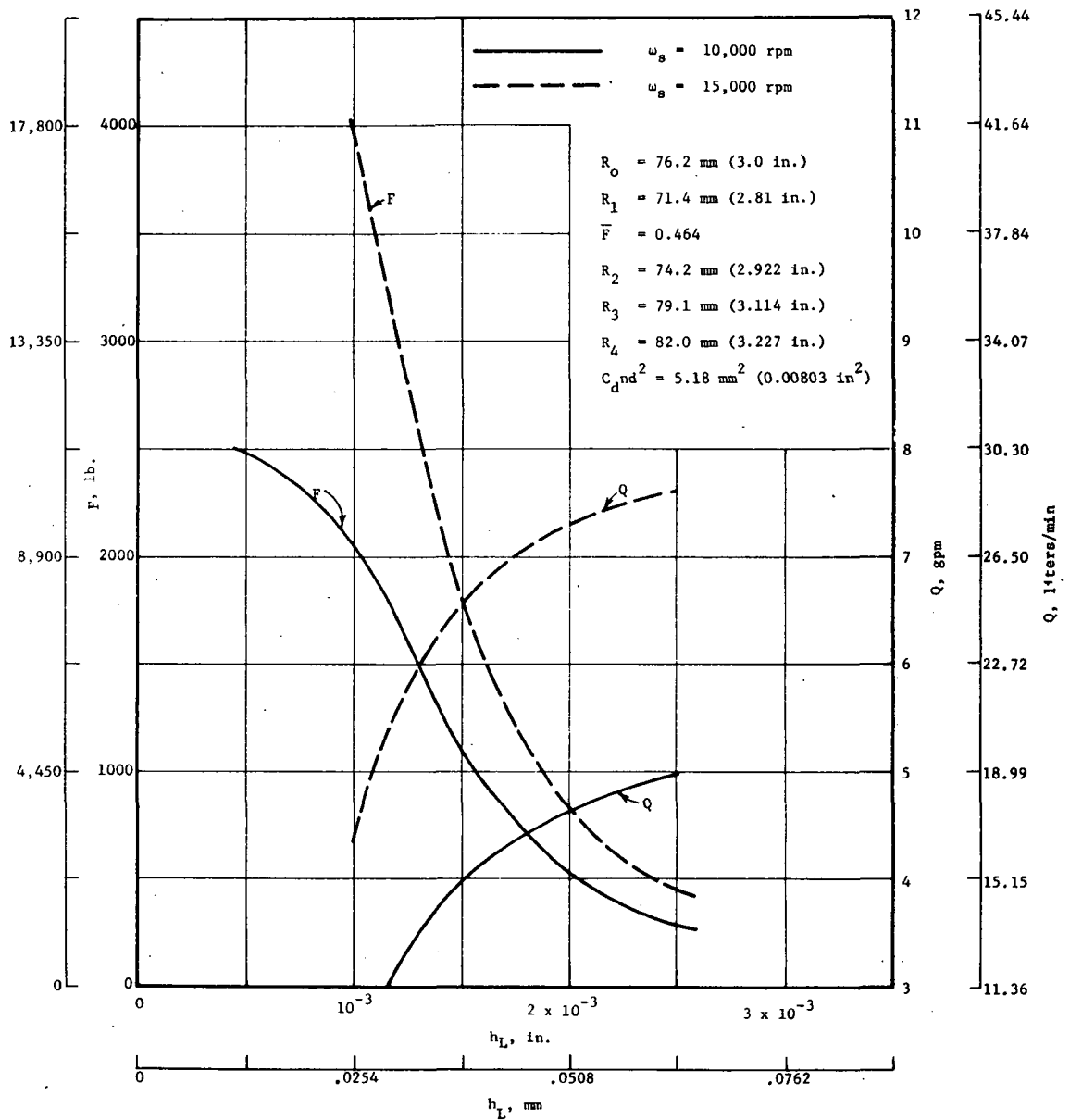


Fig. 10 Off Design Speed Performance
Load and Flow vs. Film Thickness

$$\bar{p} = 0.4$$

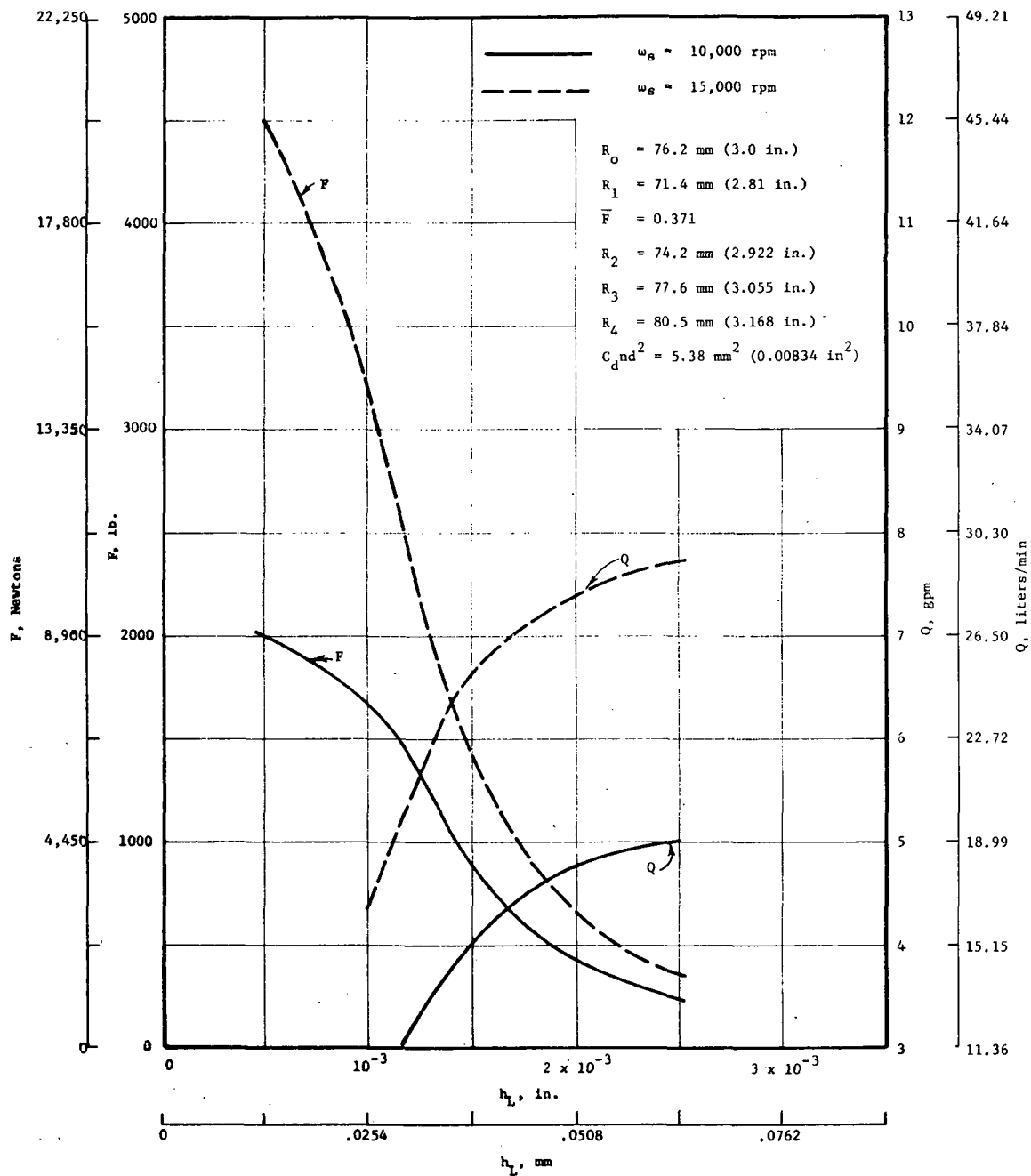


Fig. 11 Off Design Speed Performance
Load and Flow vs. Film Thickness

$$\bar{p} = 0.5$$

The selection of the pocket depth h_p involves a compromise between bearing stiffness and torque.^P High h_p/h_L values exhibit low stiffness and low torque. The inverse holds true for low values of h_p/h_L . High values of h_p/h_L require unrealistically deep pockets while low values increase the operational torque causing unfavorable speed distribution in the final bearing and high power losses. An h_p/h_L of 100 representing an average value was thus selected for this application.

The selected values of \bar{p} and h_p/h_L indirectly establish a bearing configuration of the following make-up:

Dimensionless Parameters

$$\bar{p} = 0.3$$

$$\bar{Q} = 55.50$$

$$F = 0.6189$$

Bearing Dimensions

$$R_o = 76.2 \text{ mm (3 in.)}$$

$$R_1 = 71.4 \text{ mm (2.810 in.)}$$

$$R_2 = 74.2 \text{ mm (2.922 in.)}$$

$$R_3 = 81.5 \text{ mm (3.210 in.)}$$

$$R_4 = 84.3 \text{ mm (3.319 in.)}$$

$$h_p = 0.0345 \text{ mm (0.136 in.)}$$

$$C_d n_d^2 = 5.26 \text{ mm}^2 \text{ (0.00816) in.}^2$$

$$\theta = 45^\circ$$

The selected dimensions do not appear to present problems from the manufacturing point of view, although final finishes and tolerances on squarenesses and cone angle will require particular care in manufacture as well as at assembly.

The torque versus speed ratio ω_b/ω_s curves for shaft speed of 20,000, 15,000, and 10,000 rpm are shown in Figures 12 through 14 respectively, for the selected bearing. In all figures, the load F or the clearance h_L appears as the third parameter. Ball bearing data may be cross-plotted as shown in each of these figures to obtain the equilibrium ball bearing speed. The results of this crossplot will be discussed in section II-C.

The axial stiffnesses of the selected bearing are plotted in Figure 15 for speeds of 10,000, 15,000, and 20,000 rpm. These stiffnesses were obtained by numerical differentiation of the $F - h_L$ data presented in Figures 6 and 9.

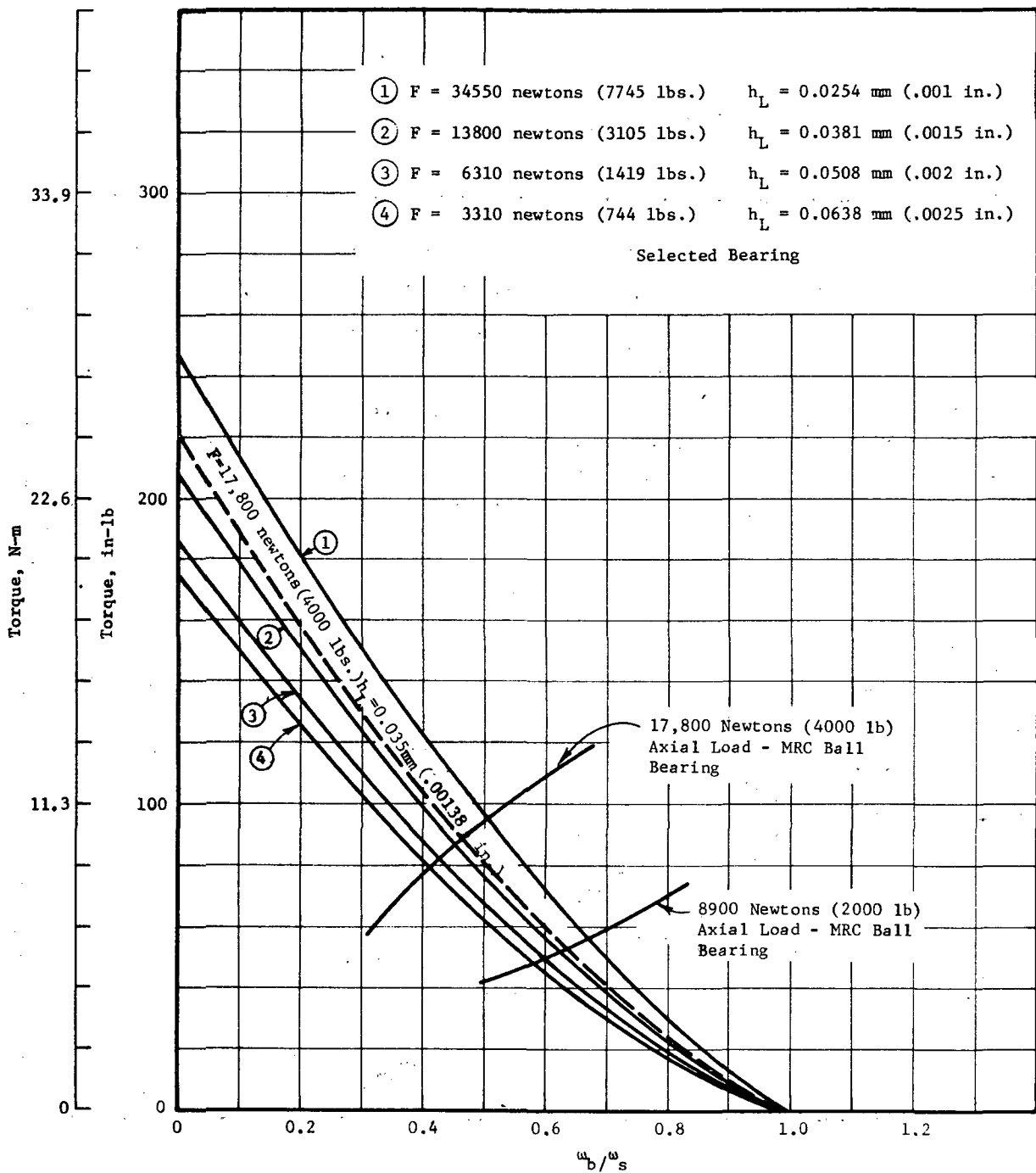


Fig. 12 Speed Split of Series Hybrid Thrust Bearing;
Speed = 20,000 rpm

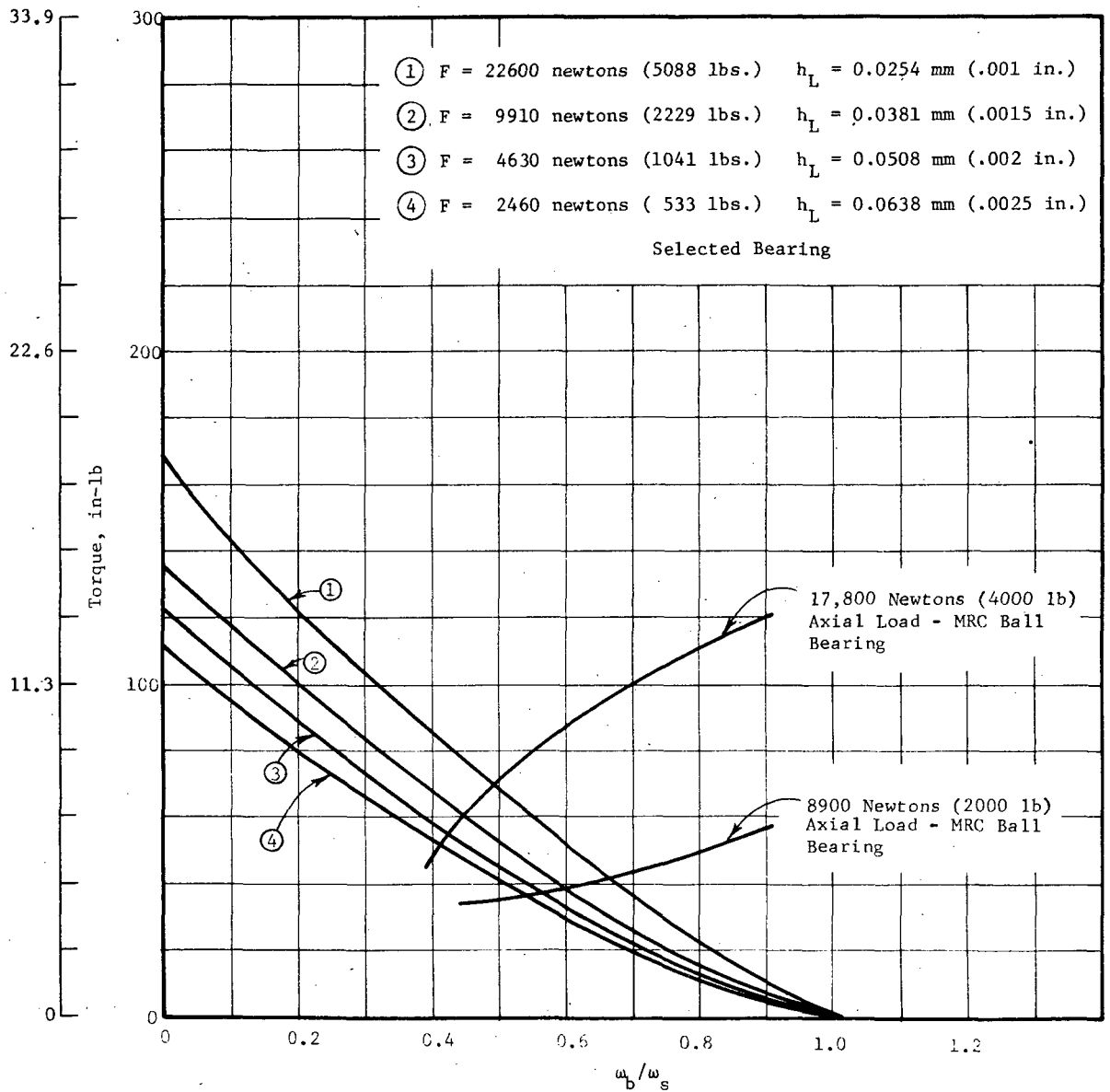


Fig. 13 Speed Split of Series Hybrid Thrust Bearing;
Speed = 15,000 rpm

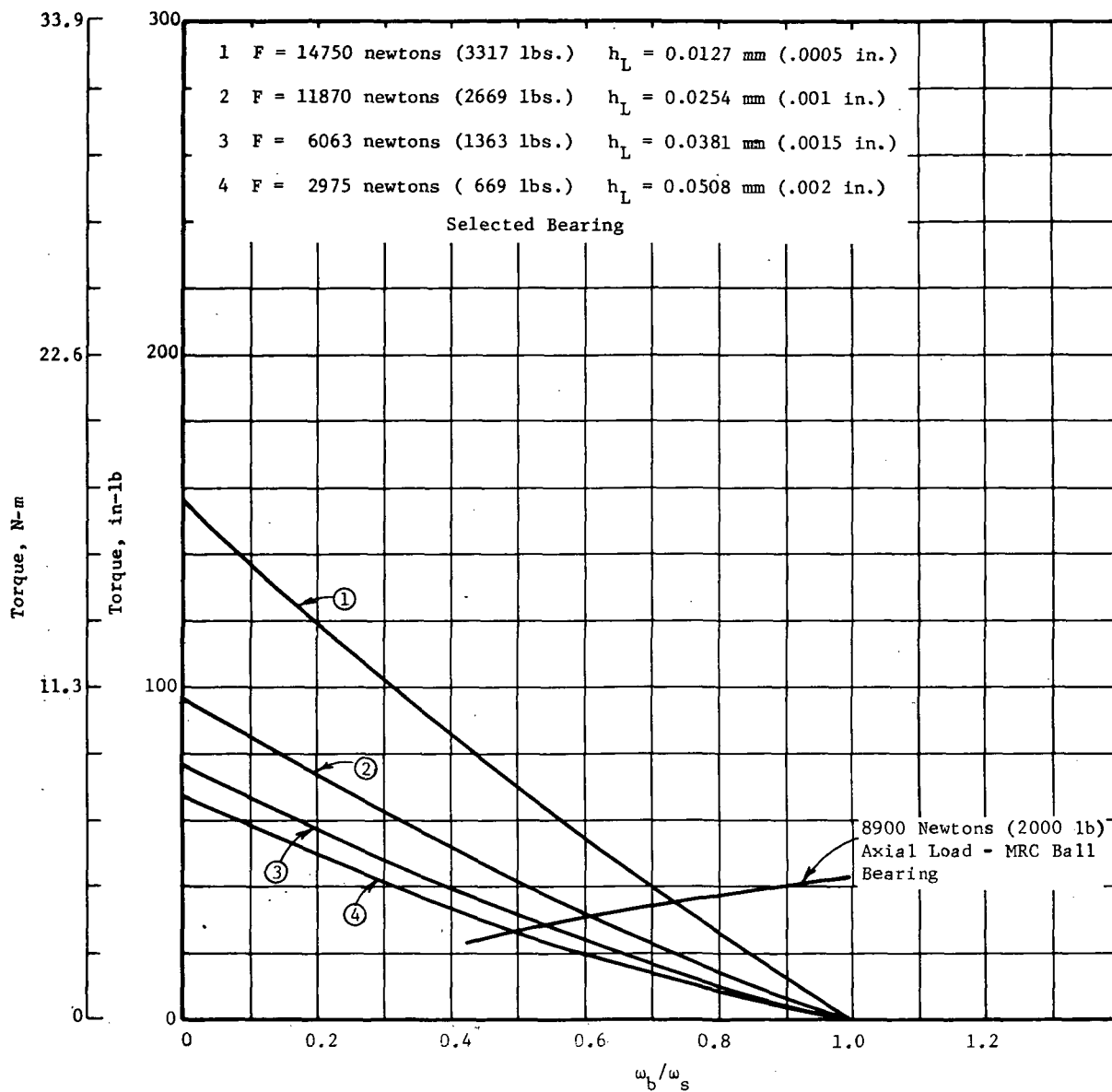


Fig. 14 Speed Split of Series Hybrid Thrust Bearing;
Speed = 10,000 rpm

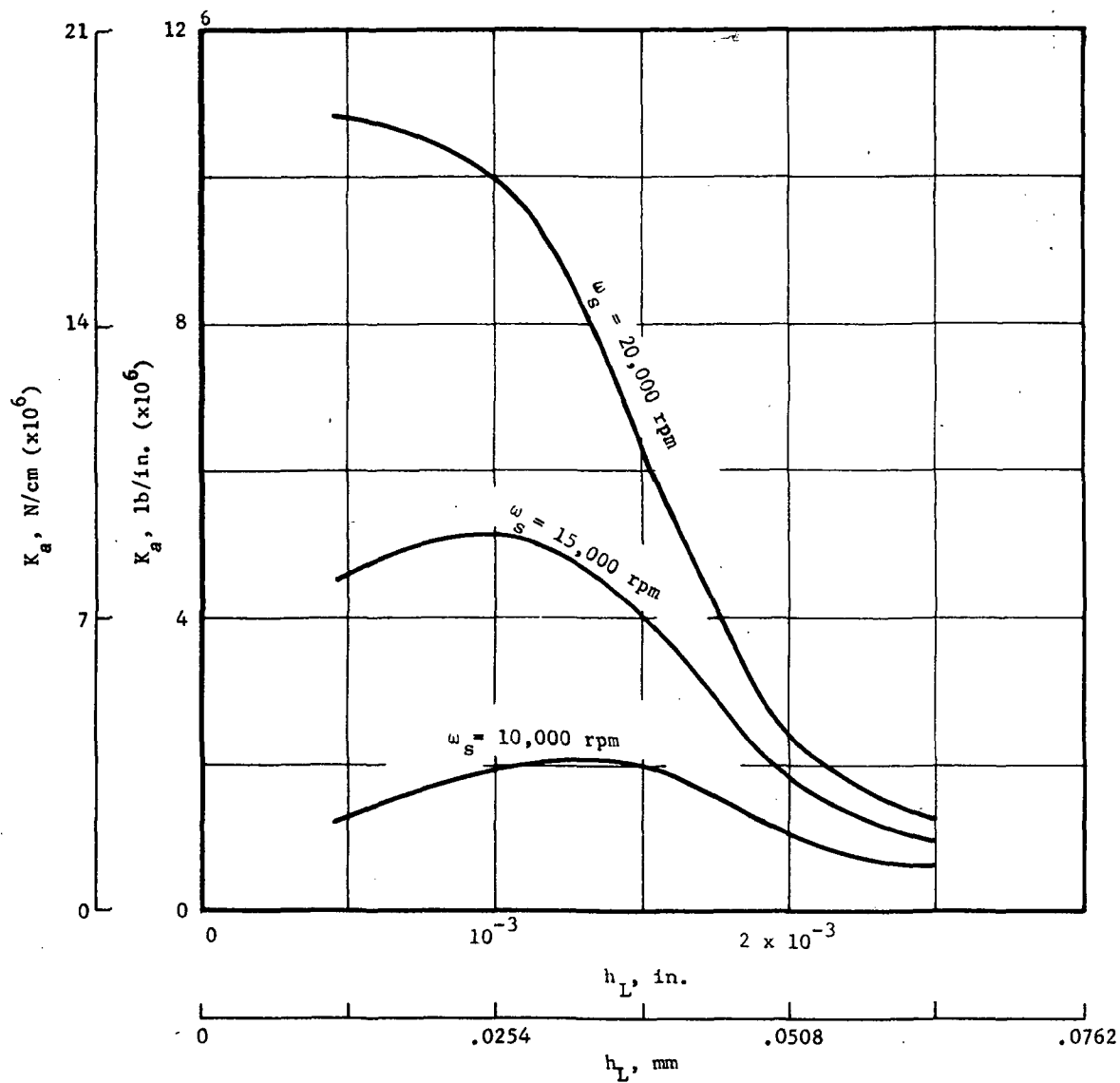


Fig. 15 Axial Stiffness of Fluid-Film Bearing

B. Ball Bearing Configuration

The 150-mm bore ball bearing configuration was provided by the NASA Project Manager. This configuration is representative of the actual ball bearing to be used in the forthcoming tests. An analysis of the ball bearing performance characteristics, in the form of computer output sheets, based on the T. A. Harris program was also provided by the NASA Project Manager, as was actual test data on full size ball bearing tests (Reference 2).

According to the test data in Reference 2, the ball bearing torque at 8900 and 17,800 newtons (2000 and 4000 lbs.) axial loading is as given in Table I. Note that, because of inconsistency in torque measurements among the test bearings, data pertaining to one specific ball bearing was selected. The reasons for this selection are two-fold. Firstly, the selected data on MRC bearing S/N 433A yields realistic torque values which increase with speed as normally anticipated, and secondly the data also appears to be reasonably close to measurements of torque obtained at MTI on similar bearings. The other bearings tested at MRC, at 367 K (200°F) oil in temperature, appear to (with minor exceptions) produce erratic torque behavior. The torque values listed in Table I will be used to calculate differential speed between the fluid-film and ball bearings.

The ball bearing radial stiffness is shown in Table II. The stiffness values were calculated on the A. B. Jones RECAP Program. The significance of the ball bearing radial stiffness in connection with the dynamic rotor stability over the full test-speed range will be discussed in a later section.

C. Series Hybrid Thrust Bearing Performance

Once the torque characteristics of the fluid-film bearing and ball bearing components are known, the performance characteristics of the combined hybrid bearing can be calculated. Inasmuch as the testing will be performed at three discrete speeds (10,000, 15,000 and 20,000 rpm) the performance characteristics of the combined bearing will be presented for each test speed. Some performance characteristics of importance to the user of a series hybrid bearing, such as the effects of speed and load on fluid-film bearing flow and film thickness, have already been discussed in the fluid-film bearing design section. The important parameters to be determined here are:

- a. Differential speed between the ball and fluid-film bearing
- b. The net benefits of the speed differentials in terms of load carrying capacity, ball bearing life, and power loss

1. Determination of Differential Speed

The split between the shaft speed and that of the ball bearing inner race can be determined from a crossplot of ball bearing and fluid-film bearing torques as a function of ball bearing speed to shaft speed ratio ω_b/ω_s . The fluid-film bearing torque characteristics

TABLE I

Ball Bearing Torque Characteristics
S/N 433A

20,000 RPM RUN					
Speed rpm	$\frac{\omega_b}{\omega_s}$	Torque			
		Newton-meters (in-lb)			
		8900 newtons (2000 lbs.) axial load		17800 newtons (4000 lbs.) axial load	
6,670	.313	3.72	(32.9)	6.38	(56.5)
10,000	.500	4.66	(41.2)	10.89	(96.4)
13,000	.665	6.27	(55.5)	13.33	(118)
15,200	.760	7.70	(68.1)	13.00	(115)
16,660	.833	8.37	(74.1)	14.57	(129)
18,330	.916	9.10	(80.5)	15.59	(138)
20,000	1.00	9.53	(84.3)	17.52	(155)

15,000 RPM RUN				
Speed ,rpm	$\frac{\omega_b}{\omega_s}$	Torque		
		Newton-meters (in-lb)		
		8900 N	(2000 lbs)	17800 N (4000 lbs.)
6,670	.445	3.72	(32.9)	6.38 (56.5)
10,000	.667	4.66	(41.2)	16.89 (96.4)
13,300	.89	6.27	(55.5)	13.33 (118)
15,200	1.01	7.70	(68.1)	13.00 (115)

10,000 RPM RUN		
Speed ,rpm	$\frac{\omega_b}{\omega_s}$	Torque
		Newton-meters (in-lb)
		(a) 8900 newtons (2000 lbs.)
6,670	.67	3.72 (32.9)
10,000	1.0	4.66 (41.2)

TABLE II

Ball Bearing Radial Stiffness

Speed rpm	Load		Stiffness [*]	
	Newtons	lb.	Newton/cm	lb/in x 10 ⁻⁵
20,000	17,800	4000	6.48	3.7
	13,350	3000	5.25	3.0
	8,900	2000	4.73	2.7
	4,450	1000	2.63	1.5
15,000	17,800	4000	6.13	3.5
	13,350	3000	4.73	2.7
	8,900	2000	3.33	1.9
	4,450	1000	1.93	1.1
10,000	17,800	4000	6.65	3.8
	13,350	3000	4.90	2.8
	8,900	2000	3.15	1.8
	4,450	1000	1.58	0.9

* Radial Stiffness was calculated on the RECAP Program.

were calculated within the scope of this design effort. The ball bearing torques were, as earlier discussed, taken from Reference 2.

The crossplot of the torque data is shown in Figures 12 - 14 for test shaft speeds of 20,000 rpm, 15,000 rpm and 10,000 rpm respectively. Note that the ball bearing torque at 8900 newtons (2000 lbs.) is approximately one-half that at 17,800 newtons (4000 lbs.). This high degree of torque dependence on load is more indicative of Coulomb friction rather than of friction existing in well lubricated bearings operating on an elastohydrodynamic film. Because of the high ball bearing torque at the 17,800 newtons (4000 lbs.) load level, the low speeds attributed to the ball bearing may be highly optimistic. According to the plots presented in Figures 12 - 14, the hybrid bearing should be capable of supporting 17,800 newtons (4000 lbs.) at shaft speeds of 20,000 and 15,000 rpm. At 10,000 rpm, the load carrying capacity drastically decreases because of the reduction in the inertia forces. At this speed, the load corresponding to a 0.0254 mm (1 mil.) film thickness is 11,900 newtons (2,669 lbs.).

Data on differential speeds extrapolated from Figures 12 - 14 is presented in Table III.

2. Net Benefits of the Speed Differential

The combination of high thrust load and high speed severely limits the ball bearing life. This limitation is difficult, and in some cases impossible to overcome with mere changes in ball bearing design and materials. The series hybrid bearing arrangement brings about a net reduction in ball bearing speed and consequently mitigates the limitations imposed by the severe operating conditions.

For example, considering the design arrived at in this report, one can evaluate the relative merits of a single ball bearing versus a hybrid bearing design. A comparison of the fatigue life and bearing power losses of the two concepts operating at 20,000 rpm within the given load range of 4450 - 17,800 newtons (1000 - 4000 lbs.) is shown in Table IV. The significant features of this comparison are high (up to ten-fold) increases in bearing fatigue life that can be obtained with the hybrid bearing at a price of a small increase in torque, and somewhat increased manufacturing complexity.

The greatest disadvantage of the hybrid bearing lies in its flow requirements. The flow consumption of the hybrid bearings at 20,000 rpm and 17,800 newtons (4000 lbs.) load is calculated to be 28.4 liters/min. (7.5 gpm) for the fluid-film bearing plus 4.54 liters/min. (1.2 gpm) for the ball bearing alone at the above conditions of operation. The increased flow, however, does not represent as great an obstacle to operation at high speeds and high loads as that presented by the inherent ball bearing fatigue life limitations.

TABLE III

Differential Speed Data

Shaft Speed ω_s rpm	Ball Bearing Speed ω_b rpm	$\frac{\omega_b}{\omega_s}$	Load	
			Newtons	(lbs.)
20,000	9200	0.46	17,800	(4000)
20,000	12200	0.61	8,900	(2000)
15,000	7000	0.48	17,800	(4000)
15,000	9600	0.64	8,900	(2000)
10,000	5900	0.59	8,900	(2000)

TABLE IV

Torque and Life Comparison Between
Single and Hybrid Bearings

Speed rpm	Load		B ₁₀ [*] hrs.		Torque Newton-meters (in-lb)	
	Newton	(lbs.)	Simple	Hybrid	Simple	Hybrid
20,000	17,800	(4000)	100	1150	17.5 (155)	19.9 (176)
20,000	8,900	(2000)	139	1750	9.5 (84)	11.3 (100)
15,000	17,800	(4000)	406	1350	13.0 (115)	14.2 (126)
15,000	8,900	(2000)	821	6400	7.7 (68)	9.0 (80)

*The B₁₀ life is calculated on the basis of air melted material constants and does not include elastohydrodynamic or vacuum melted material correction factors.

D. Thermal Analysis

As part of the hybrid bearing analysis, an evaluation of the temperature distributions within the critical bearing areas was performed.

Thermal mapping calculations were made with a 367°K (200°F) inlet oil temperature, the maximum 17,800 newtons (4000 lbs.) load (Minimum film thickness at the fluid-film bearing) and speed of 20,000 rpm.

Included in the analysis were the heat inputs due to both ball bearing and fluid-film bearing friction, as well as the effects of oil flow to both bearings.

The finite element thermal model utilized in the temperature mapping study for the Series Hybrid boost configuration is shown in Figure 16. Boundary condition types and forced convection flows are located as indicated. Since the computer program input provides for non-orthogonal surfaces, the bearing surfaces can be modeled as they actually appear.

The boundary condition values for the 367°K (200°F) lubricant inlet temperature are shown in Table V with the resulting thermal mapping calculations presented in Figure 17.

Indicative of a satisfactory design configuration are the relatively low axial and radial thermal gradients which exist in both runner and stator.

Lubricant flows through both the ball bearing and the fluid-film bearing serve the important function of heat removal, judging by the 11°K (20°F) temperature rise in the ball bearing lubricant flow and a similar rise in the fluid-film lubricant temperature.

The peak metal temperatures for the 367°K (200°F) lubricant inlet condition appear at the ball bearing with slightly lower temperatures occurring at the fluid-film bearing. In general, the predictions appear reasonable and no indications of any significant temperature gradients which would affect operation of the series hybrid boost bearing configuration are apparent.

E. Thermoelastic Deformation Analysis

Thermoelastic deformation calculations were performed for both the runner and stator of the series hybrid boost bearing configuration. Each component was subjected to a 17,800 newtons (4000 lbs.) thrust load and used the 367°K (200°F) lubricant inlet temperature thermal distribution calculated for the 20,000 rpm main rotor speed.

The additional effect of centrifugally induced forces due to the high rotational speed is also included in the deformation analysis.

The thermoelastic deformation model for the primary rotor calculation is shown in Figure 18. The axis of revolution for this model is at the identified centerline. The active thrust area at the fluid-film bearing is

- ① - ⑥ ; Flow Streams

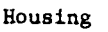


Fig. 16 Mathematical Model for Heat Transfer

TABLE V
THERMAL MODEL SPECIFICATIONS FOR SERIES HYBRID BOOST BEARING

Primary Rotor Speed	20,000 rpm
Intermediate Rotor Speed	10,000 rpm
Inlet Oil Temperature (All Brgs.)	367 °K (200°F)
Inlet Oil Viscosity	5.5×10^{-3} N/sec-m ² (8×10^{-7} lb-sec/in ²)
Inlet Oil Pressure	As Required

LUBRICANT FLOW DATA

Flow Stream Number	Flow Rate		Specific Heat	
	liters/min	(gpm)	joules/Kg - °K	(Btu/lb - °F)
I	31.0	(8.2)	2.34×10^{-4}	(.56)
II	31.0	(8.2)	2.34×10^{-4}	(.56)
III	3.8	(1.0)	2.34×10^{-4}	(.56)
IV	3.8	(1.0)	2.34×10^{-4}	(.56)
V	3.8	(1.0)	2.34×10^{-4}	(.56)
VI	3.8	(1.0)	2.34×10^{-4}	(.56)

HEAT GENERATION RATES

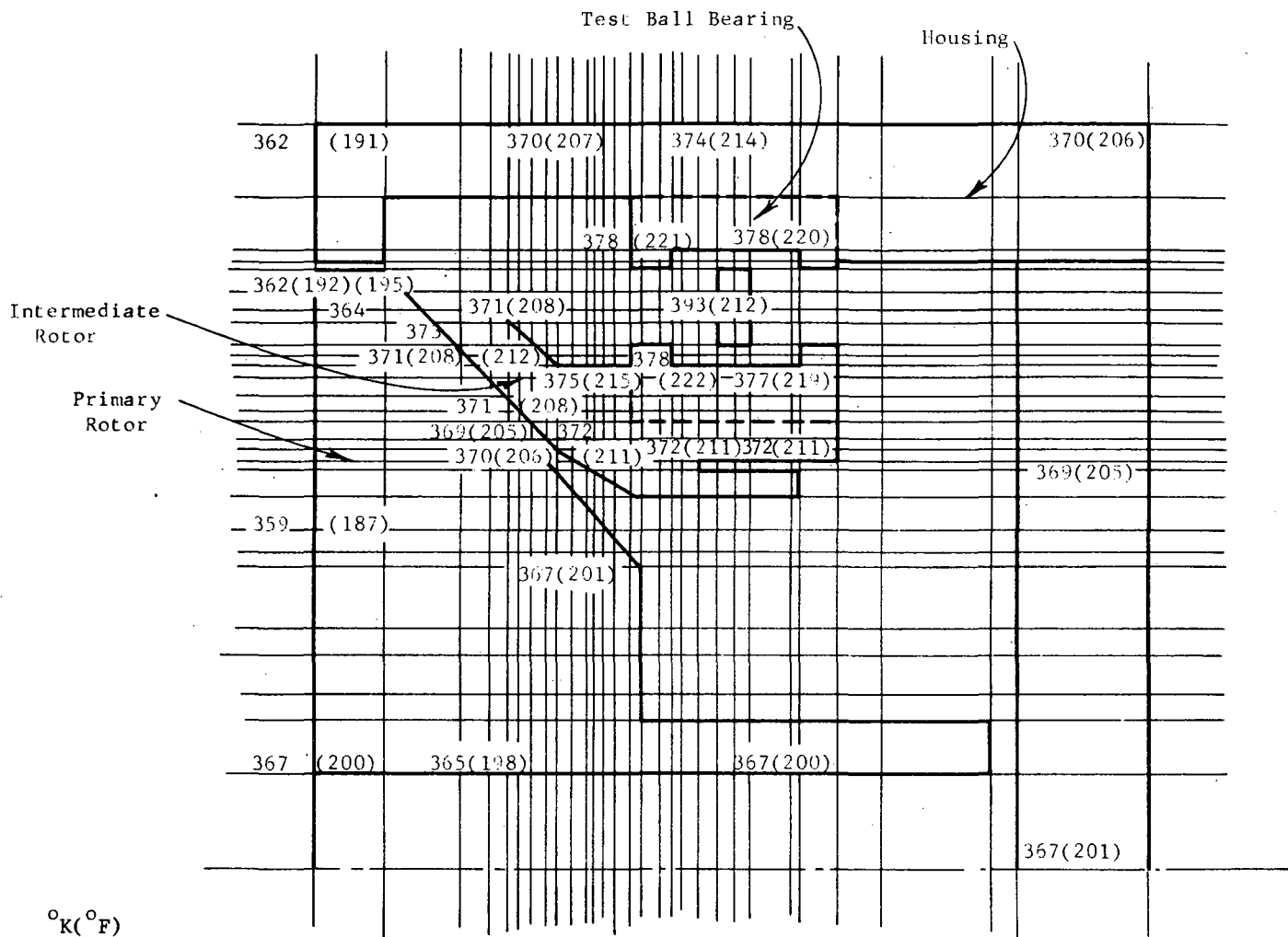
Location	Heat Rate	
	watt/m ²	(Btu/hr-ft ²)
Ball Bearing	12.9×10^5	(4.1×10^5)
Fluid-Film Bearing	16.5×10^5	(5.25×10^5)
Windage	31.5×10^3	(10×10^3)

BOUNDARY CONDITIONS

Location	Type	Temperature		Film Coefficient	
		°K	(°F)	watt/meter ² -°K	(Btu/hr-ft ² °F)
A	Insulated	---	---	--	--
B	Forced Convection	367	(200°F)	255	(45)
C	Fixed Temperature	367	(200°F)	--	--
D	Fixed Temperature	367	(200°F)	--	--
E	Free Convection	300	(80°F)	397	(70)
F	Free Convection	300	(80°F)	22.7	(4)
G	Free Convection	300	(80°F)	22.7	(4)
H	Forced Convection	367	(200°F)	1985	(350)

MATERIAL CONSTANTS

Identification No.	Thermal Conductivity	
	watts/m - °K	(Btu/hr-ft - °F)
1	4.16×10^{-5}	(0.016)
2	16.64×10^{-3}	(6.4)
3	20.8×10^{-3}	(8.0)
4	16.9×10^{-3}	(6.5)
5	15.6×10^{-3}	(6.0)
6	13×10^{-3}	(5.0)
7	10.4×10^{-3}	(4.0)
8	8.32×10^{-3}	(3.2)
9	24.96×10^{-3}	(9.6)
10	7.54×10^{-3}	(2.9)
11	24.96×10^{-3}	(9.6)
12	29.12×10^{-3}	(11.2)
13	24.96×10^{-3}	(9.6)
14	58.24×10^{-3}	(22.4)
15	16.64×10^{-3}	(6.4)



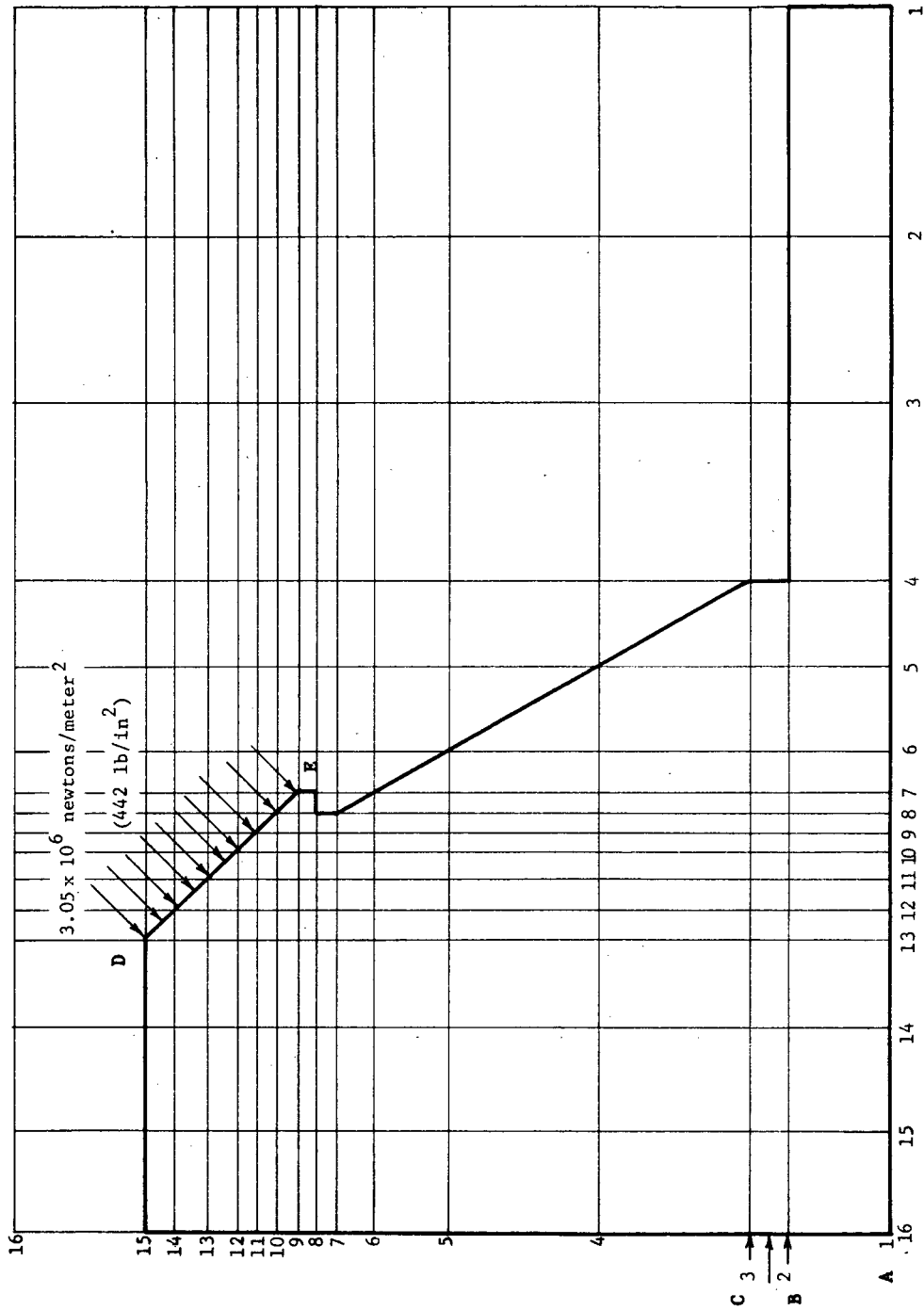


Fig. 18 Thermoelastic Model for Fluid-Film Bearing
Primary Rotor

located between model points and arrows. Axial restraint is provided at the lower left corner and radial restraint at the inner radius, as shown. Bearing pressure loading is as indicated by arrows at the appropriate locations. Table VI lists the input parameters used in the final distortion calculation. These are identified on Figure 18 with the appropriate number or letter.

The temperature distribution imposed on the analytical model is provided by the results of the thermal analysis given previously. Pressure loadings due to the imposition of axial loads and the effects of rotation are included as input to the thermoelasticity computer calculations.

It should be pointed out that the listed inputs represent the maximum operating conditions for both load and speed and, therefore, imposed the most severe requirements on the fluid-film bearing.

The intermediate rotor (model shown in Figure 19) was also subjected to a thermoelastic deformation analysis using the temperatures developed during the thermal analysis. In general, the remainder of the inputs are identical to the primary rotor with the exception that a 10,000 rpm speed is used for generating body forces. The listing of inputs for the intermediate rotor is shown in Table VII.

The objective of the distortion analysis for the combined loading and temperature distributions was to determine the extent of all the possible distortion producing effects on the parallelism of the fluid-film bearing.

The calculated results of the distortion analysis show that both rotor members remain conical although a nominal radial growth and rotation of both the primary and intermediate bearing faces occurs. The net effect, however, is only a slight decrease in the outer edge film thickness.

Table VIII shows the combined distortion calculation results for both bearings. The net angular distortion of 0.00013 radians corresponds to a net loss of less than 2.54×10^{-3} millimeters (0.0001 in.) in film thickness at the outer edge of the fluid-film bearing.

On the basis of the foregoing results, the degradation in conical bearing performance that results because of deformations at or near the bearing surfaces, should be negligibly small.

TABLE VI

INPUT PARAMETERS
PRIMARY ROTOR DISTORTION ANALYSIS

<u>Item</u>	<u>Property</u>
Location A	Restrained from axial movement
Location B to C	$27.6 \times 10^6 \text{ N/m}^2$ (4000 psi) (distributed)
Location D to E	$3.05 \times 10^6 \text{ N/m}^2$ (442 psi) (distributed)
Speed	20,000 rpm
Density	$7.83 \times 10^3 \text{ Kg/m}^3$ (.283 lb/in ³)
Young's Modulus	$207 \times 10^9 \text{ N/m}^2$ ($30.0 \times 10^6 \text{ lb/in}^2$)
Poisson's Ratio	0.3
Thermal Expansion Coefficient	$15.1 \text{ m/m } ^\circ\text{K}$ ($8.4 \times 10^{-6} \text{ in/in } ^\circ\text{F}$)

TABLE VII

INPUT PARAMETERS
INTERMEDIATE ROTOR DISTORTION ANALYSIS

<u>Item</u>	<u>Property</u>
Location A	Restrained from axial movement
Location B to C	$6.78 \times 10^6 \text{ N/m}^2$ (984 psi) (distributed)
Location D to E	$3.05 \times 10^6 \text{ N/m}^2$ (442 psi) (distributed)
Speed	20,000 rpm
Density	$7.83 \times 10^3 \text{ Kg/m}^3$ (2.83 lb/in ³)
Young's Modulus	$207 \times 10^9 \text{ N/m}^2$ ($30.0 \times 10^6 \text{ lb/in}^2$)
Poisson's Ratio	0.3
Thermal Expansion Coefficient	$15.1 \text{ m/m } ^\circ\text{K}$ ($8.4 \times 10^{-6} \text{ in/in } ^\circ\text{F}$)

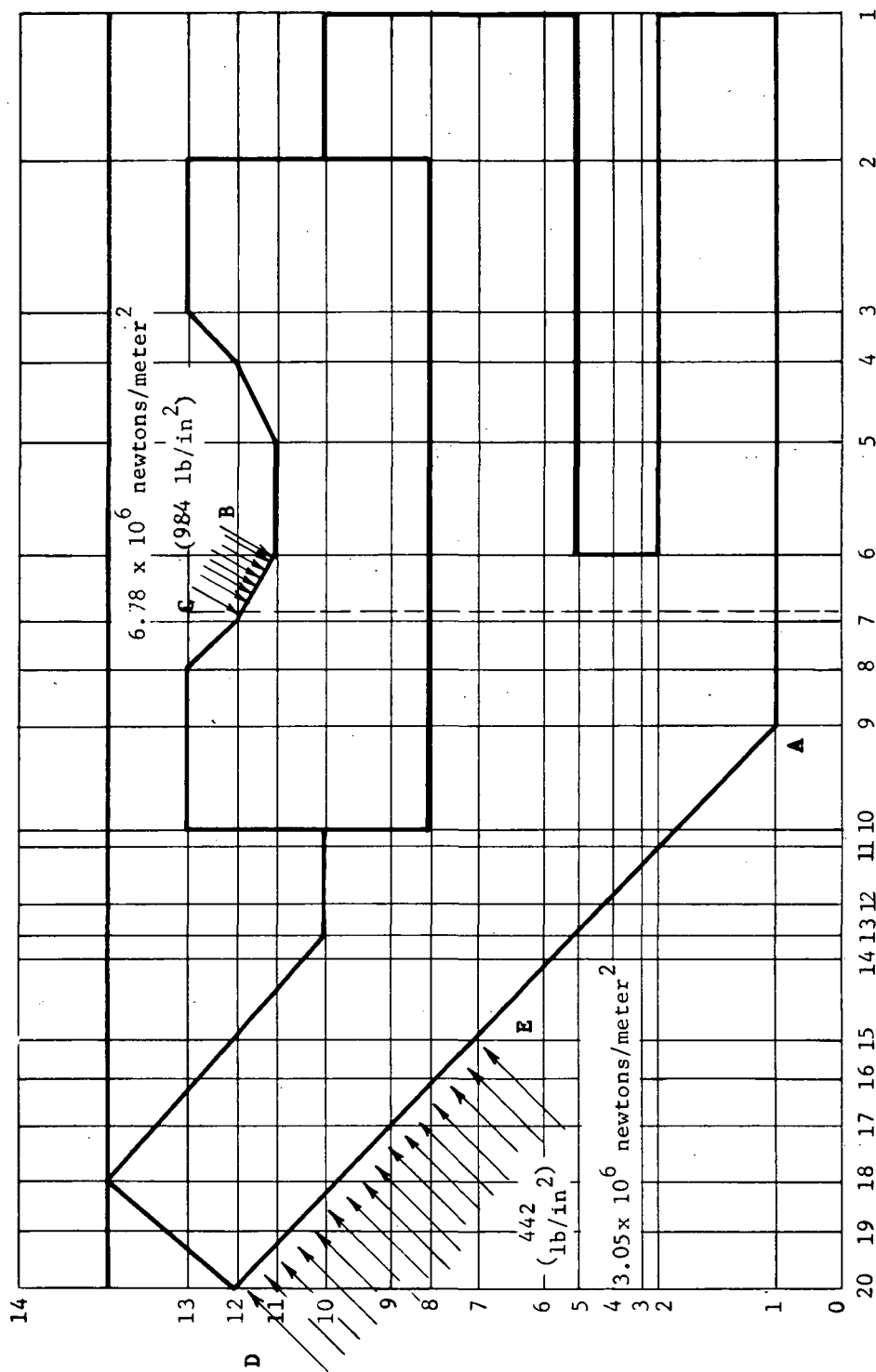


Fig. 19 Analytical Model for the Intermediate Rotor

TABLE VIII

SUMMARY OF DISTORTIONS
FLUID-FILM BEARING

Coordinates	Original mm (in)	Displacements (10^{-3} mm) (in)		Net Change (10^{-3} mm) (in)
		Spindle	Middle Rotor	
Inner Edge	Radial	50.8 (2.001)	5.5 (-.218)	
	Axial	88.3 (3.477)	103 (4.047)	14.5 (.570)
Outer Edge	Radial	44.2 (1.739)	16.5 (-.649)	
	Axial	110 (4.344)	127 (5.012)	17.0 (.668)
Relative Angle	25.4 (1)	25.9 (1.01927) rad	25.9 (1.01914) rad	0.003 (.00013) rad

III. CRITICAL SPEED ANALYSIS

Investigations of the critical speed and rotor response for the Series Hybrid Bearing test vehicle as initially designed, disclosed the presence of a critical speed at 20,000 rpm. Since this represents a speed at which test data will be taken, modifications had to be made in the design to shift this critical speed out of the operating range.

A stiffened test ball bearing seat and a minimum limit in test ball bearing stiffness of 3.50×10^5 N/cm (2×10^5 lb/in) removed this critical speed from within the test speed range. A low critical speed at approximately 9000 rpm which is dependent on the primary rotor mass and support bearing stiffness, however, still exists. Studies of the response of a three-level system assigning all primary rotor parts to level one, the intermediate rotor and test ball bearing to level two, and the stationary test housing to level three, still indicated a serious resonance existed at or near 20,000 rpm due to the excitation of the low-speed primary rotor critical by the rotation of the intermediate rotor (which operates at one-half the primary rotor speed).

The final response study now indicates that stable performance can be achieved at 20,000 rpm and that insignificant response amplitudes occur at all other test speeds when the front end spindle bearing is flexibly mounted with a system which also includes a damper.

Figure 20 shows the critical speed map for the final rotor design. Curve (A) is the critical speed associated with the primary rotor. It is this critical that was excited by the one-half speed rotation of the intermediate rotor. Curve (B) represents a resonant condition of the intermediate rotor which is independent of the test ball bearing stiffness and does not exist above a fluid-film stiffness of 8.75×10^4 N/cm (5×10^4 lb/in). Curve (C) shows the critical speed of the intermediate rotor which is independent of the fluid-film bearing stiffness. This is the critical speed which is maintained above the test rigs required speed range by holding the ball bearing stiffness above 3.50 N/cm (2×10^6 lb/in).

The results of synchronous unbalance response indicate a maximum amplitude at the fluid-film bearing of 4.83×10^{-3} mm (0.19×10^{-3} in.) peak-to-peak at 9000 rpm can be caused by an unbalance of 0.0072 N/cm (0.01 oz-in) at the spindle coupling that is out of phase with a 0.0072 N/cm (0.01 oz-in) unbalance at the bearing. The maximum relative eccentricity, however, is less than .051 mm (.002 in.) and this occurs only at 20,000 rpm.

Since both residual unbalances will be held to much lower levels than were used in the calculation, the low response values and the absence of significant critical speeds within the testing matrix permitted the test rig design to be frozen and committed to final detailing.

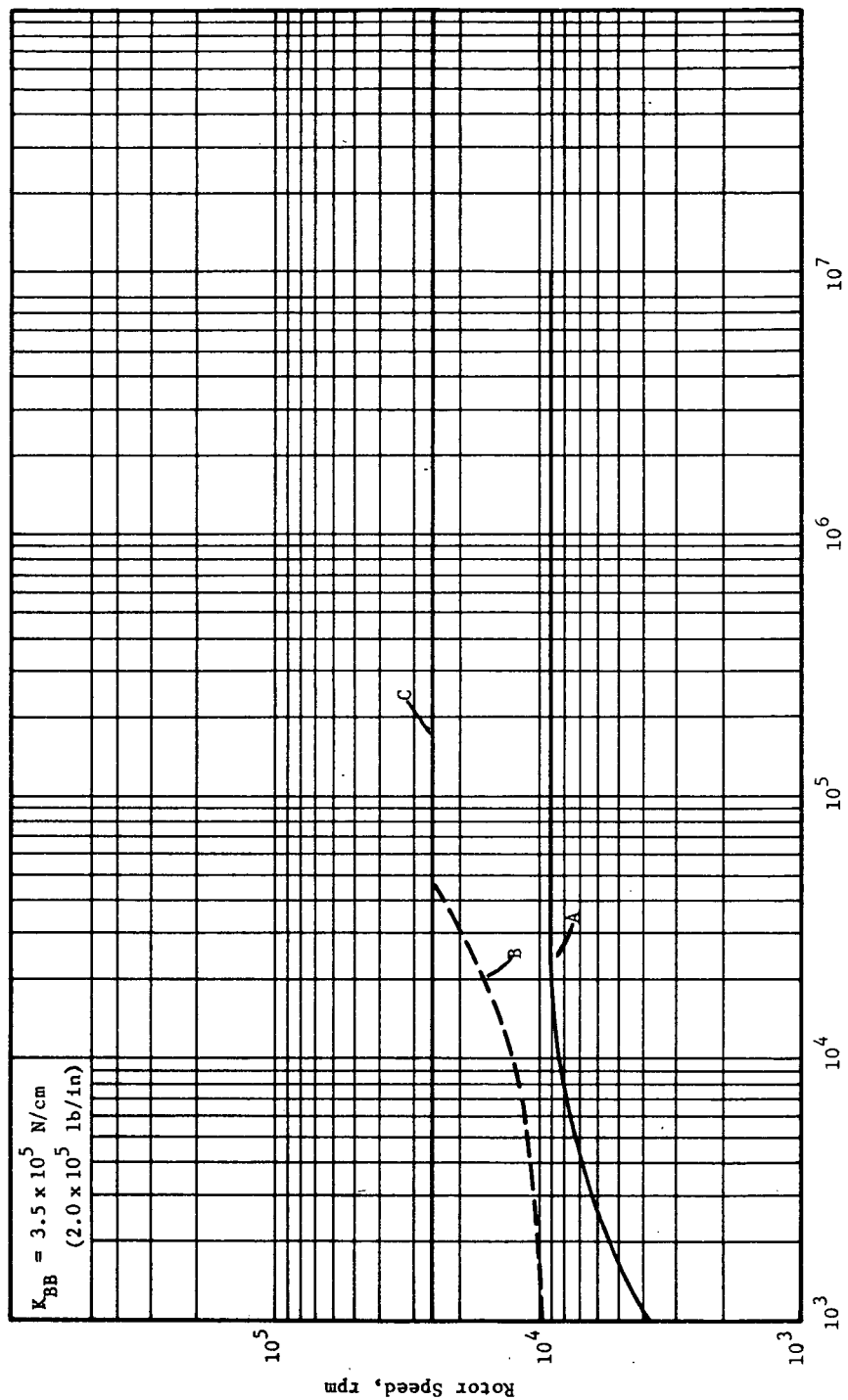


Fig. 20 Fluid-Film Bearing Stiffness, x 1.75 Newtons/cm (lbs./in.)

IV. DESCRIPTION OF BEARING AND TEST VEHICLE

The test vehicle consists of a spindle formerly employed in the NASA Hybrid Bearing Tests (Reference 3), the shaft of which protrudes at one end to permit the mounting of the new Series Hybrid Bearing test head. The layout of the Series Hybrid Bearing arrangement is shown in Figure 21.

In the Series Hybrid Bearing design, the ball bearing ① is placed in series with a fluid-film bearing consisting of an intermediate member ② and a shaft member ③. The intermediate member is affixed to the ball bearing inner race and rotates at the same speed. The shaft member is fixed to the spindle shaft ④ and rotates at the spindle driving speed. The ball bearing outer race is mounted in the outer housing ⑤, the outer housing being provided with an end cover ⑥. The end cover contains a guide bushing ⑦ which is used mainly for augmenting the initial alignment between the fluid-film bearing parts. Oil is supplied to the center of the shaft through an oil tube ⑧, and is directed via radial passages ⑨ to the fluid-film bearing orifices ⑩ and subsequently into the fluid-film bearing area. Oil to the ball bearing is supplied through an oil jet ⑪ into an annular opening located in the intermediate member ②.

The speed of rotation of the intermediate member ② is measured with speed pick-up ⑫. A photonic sensor ⑬, manufactured by MTI, will be used to pick-up the speed of the ball bearing cage. The speed of rotation of the input shaft will be measured on the far end of the spindle where provisions are now in existence for input speed measurements. The effectiveness of the film separating the intermediate member ② from the shaft member ③, i.e., the film thickness of the conical bearing, will be measured with inductance probes mounted in mutually parallel locations within a set of planes orthogonal to the bearing surface. One probe ⑭ will be using as its gaging surface the back of the intermediate member parallel to the bearing face area. The other probe ⑮ will gage directly off the extended conical bearing surface of the shaft member ③. In order to obtain the thickness of the oil film separating the two bearing surfaces, the differences in probe readings will be recorded at the static point of contact. Any subsequent changes in the net difference between the probe read-outs will be indicative of changes in the fluid-film thickness and hence will be representative of an actual measurement of the thickness of the oil film separating the two bearing surfaces. Four sets of probes spaced 90° apart will be used.

Thermocouples will be located in all oil inlet as well as oil discharge lines. Two thermocouples placed 180° apart ⑯ will be inserted to measure the bearing outer race temperature during operation. Each one of the inductance probes employed in the fluid-film bearings will also be accompanied by a thermocouple for local read-outs in probe temperatures. The latter is absolutely necessary in order to compensate for errors in probe output introduced by temperature variation in the vicinity of the probes.

The oil discharge from the ball bearing takes place through both ends which are exposed to the sump cavity, hence there is no foreseeable obstruction in the oil flow down to the bottom of the housing and to the discharge of the

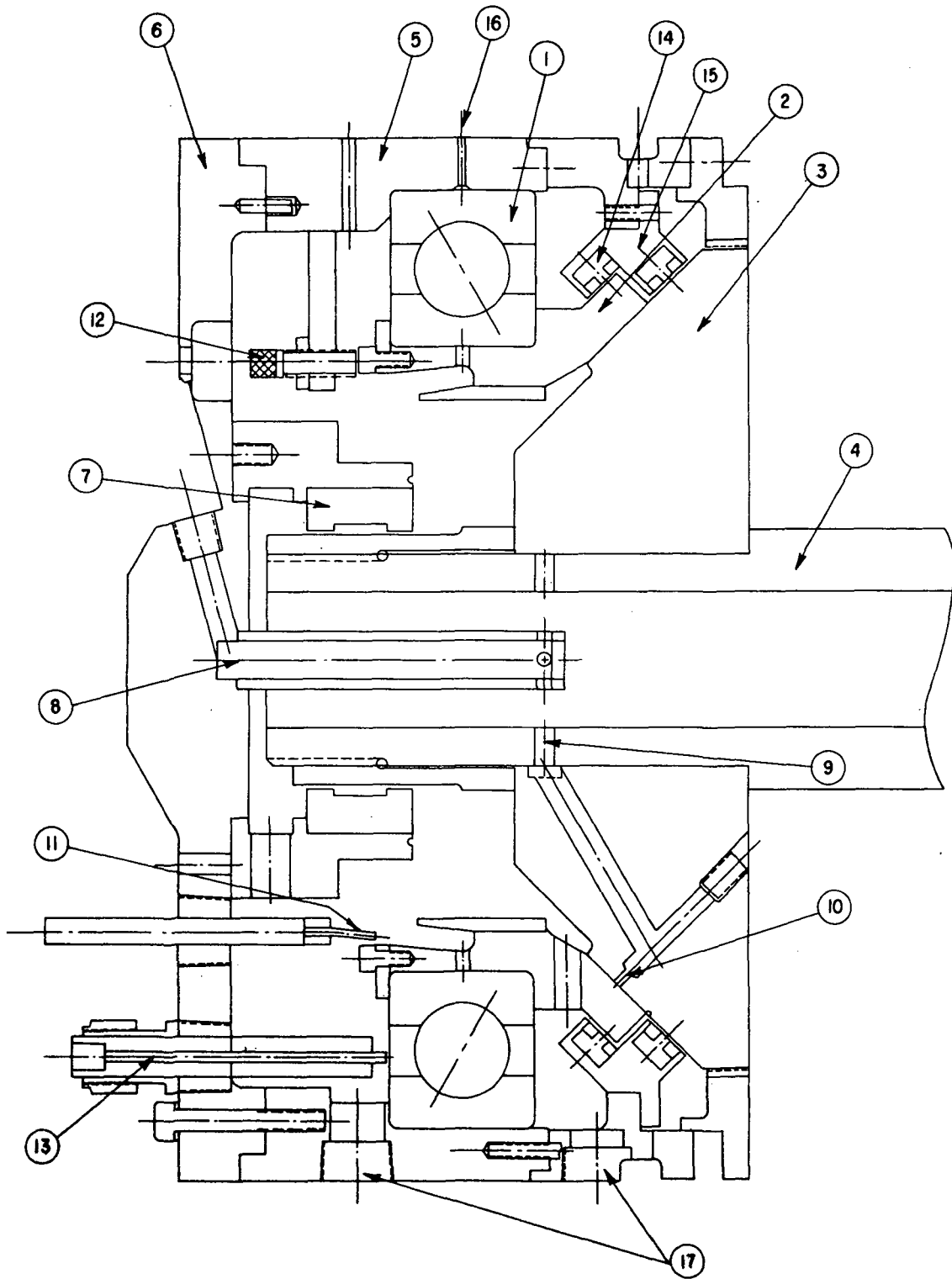


Fig. 21 Series Hybrid Bearing Test Head Layout

oil through 9.5 mm (3/8 in.) pipe fittings (17) which represent the connections to the scavenge pumps. The outer periphery of the fluid-film bearing is similarly unrestricted in permitting the flow discharging through the outer periphery to be scavenged out through the ports located at the bottom of the housing. The inner periphery of the fluid-film bearing would have a tendency to become trapped by virtue of the centrifugal field in existence between the two rotating members. In order to permit scavenge of oil emanating from the inner periphery, radial holes have been drilled in the intermediate member of the fluid-film bearing. These holes should permit quick evacuation of the trapped oil zones directly into the bearing sump, and subsequent forced drainage of the oil through the scavenge pumps.

V. CONCLUSIONS

1. The design and optimization studies of the fluid-film bearing yielded a bearing which theoretically meets all initially stipulated requirements.
2. The ball bearing torque, as measured in a series of ball bearing tests, appears to be higher than normally anticipated. Because of the higher torque, the speed split between the fluid-film bearing and the rolling-element bearing is very favorable. The speed ratio at the design point of 17,800 newtons (4000 lbs.) axial load and 20,000 rpm is approximately 0.50, indicating that the ball bearing will be operating at one-half the rotor speed at these conditions.
3. The fatigue life calculated for the ball bearing at the full-speed conditions of 20,000 rpm is approximately 1/10 of the ball bearing fatigue life calculated on the basis of the speed reduction anticipated within the series bearing setup.
4. The calculated thermal gradients across the fluid-film bearing parts are small, resulting in negligible distortion of the fluid-film bearing faces.
5. The critical speed response of the bearing test setup is greatly improved through the insertion of a spring damper support in the forward spindle bearing. Calculations indicate that safe operation throughout the specified speed range can be obtained with maximum rotor excursions not exceeding .05/mm (.002 in.) an unbalance of 0.0072 N/cm (.01 oz-in).
6. No major problems are anticipated at this time in the test and evaluation phase which follows the design phase.

NOMENCLATURE

C_d	Orifice discharge coefficient
C_1	Dimensionless laminar friction coefficient, $4 h_L \text{ fr}/h_p$
C_2	Dimensionless turbulent friction coefficient, $0.026/\text{fr} [\rho R_1 (\omega_s - \omega_b) h_p / \mu]^{0.75} h_L / h_p$
d	Orifice Diameter
F	Thrust Load
\bar{F}	Dimensionless Thrust Load, $F/(\pi p R_1^2)$
fr	Fraction of area between R_2 and R_3 occupied by hydrostatic pockets
h_L	Fluid-Film Thickness
h_p	Hydrostatic Pocket Depth
k	Fluid-Film resistance ratio, $(2 \rho p_s / 9)^{0.5} h_L^3 \sin \theta / (C_d n d^2 \mu) [1/\ln X_2 + 1/\ln (X_4/X_3)]$
M_L	Land Fluid-Film Bearing Torque
\bar{M}_L	Dimensionless Land Fluid-Film Bearing Torque, $2 M_L h_L \sin \theta / [\pi \mu (\omega_s - \omega_b) R_1^4]$
M_p	Pocket Fluid-Film Bearing Torque
\bar{M}_p	Dimensionless Pocket Fluid-Film Bearing Torque, $2 M_p h_L \sin \theta / [\pi \mu (\omega_s - \omega_b) R_1^4]$
M_t	Total Fluid-Film Bearing Torque, $M_L + M_p$
n	Number of Feeding Orifices
p	Pocket Pressure
\bar{p}	Dimensionless Pocket Pressure, p/p_s
p_s	Supply Pressure
Q	Fluid Flow
\bar{Q}	Dimensionless Fluid Flow, $6 \mu Q / (\pi p h_L^3 \sin \theta)$

NOMENCLATURE (Continued)

R_e	Reynolds Number, $\rho R_2 (\omega_s - \omega_b) h_p / \mu$
R_o	Radial location of feeding orifices
R_1	Inner Radius of Inner Land
R_2	Outer Radius of Inner Land
R_3	Inner Radius of Outer Land
R_4	Outer Radius of Outer Land
X_2	R_2/R_1
X_3	R_3/R_1
X_4	R_4/R_1
θ	Half-angle of conical hydrostatic bearing
μ	Fluid Viscosity
ρ	Fluid Density
ω_b	Ball Bearing Speed
ω_s	Shaft Speed

REFERENCES

1. Nypan, L. J., Hamrock, B. J., Scibbe, H. W. and Anderson, W. J., "Optimization of Conical Hydrostatic Bearing for Minimum Friction", J. Lubr. Tech., Vol. 94, No. 2, April 1972, pp 136 - 142.
2. Scibbe, H. W. and Munsen, H. E., "Experimental Evaluation of 150-mm Bore Ball Bearings to 3-Million DN Using Either Solid or Drilled Balls", NASA TMX-68265, Technical Paper to be presented at the Joint ASLE-ASME Lubrication Conference, Atlanta, Georgia, October 1973.
3. Winn, L. W. and Eusepi, M. W., "Development of a High-Speed Parallel Hybrid Boost Bearing", NASA CR-2226, March 1973.



POSTMASTER: If Undeliverable (Section 158
Postal Manual) Do Not Return

"The aeronautical and space activities of the United States shall be conducted so as to contribute . . . to the expansion of human knowledge of phenomena in the atmosphere and space. The Administration shall provide for the widest practicable and appropriate dissemination of information concerning its activities and the results thereof."

—NATIONAL AERONAUTICS AND SPACE ACT OF 1958

NASA SCIENTIFIC AND TECHNICAL PUBLICATIONS

TECHNICAL REPORTS: Scientific and technical information considered important, complete, and a lasting contribution to existing knowledge.

TECHNICAL NOTES: Information less broad in scope but nevertheless of importance as a contribution to existing knowledge.

TECHNICAL MEMORANDUMS: Information receiving limited distribution because of preliminary data, security classification, or other reasons. Also includes conference proceedings with either limited or unlimited distribution.

CONTRACTOR REPORTS: Scientific and technical information generated under a NASA contract or grant and considered an important contribution to existing knowledge.

TECHNICAL TRANSLATIONS: Information published in a foreign language considered to merit NASA distribution in English.

SPECIAL PUBLICATIONS: Information derived from or of value to NASA activities. Publications include final reports of major projects, monographs, data compilations, handbooks, sourcebooks, and special bibliographies.

TECHNOLOGY UTILIZATION PUBLICATIONS: Information on technology used by NASA that may be of particular interest in commercial and other non-aerospace applications. Publications include Tech Briefs, Technology Utilization Reports and Technology Surveys.

Details on the availability of these publications may be obtained from:

SCIENTIFIC AND TECHNICAL INFORMATION OFFICE

NATIONAL AERONAUTICS AND SPACE ADMINISTRATION
Washington, D.C. 20546